Edited by
Francesco S. Pavone

Laser Imaging and Manipulation in Cell Biology

WILEY-VCH Verlag GmbH & Co. KGaA

7
Light–Tissue Interaction at Optical Clearing

Elina A. Genina, Alexey N. Bashkatov, Kirill V. Larin, and Valery V. Tuchin

7.1
Introduction

This chapter describes the fundamentals and advances in controlling tissue optical properties. The scattering properties of a tissue can be effectively controlled by providing matching of refractive indices of the scatterers and the ground material (i.e., optical immersion) and/or by a change of packing parameter, and/or scatterer sizing.

The reduction of light scattering by a tissue improves the image quality and precision of spectroscopic information, decreases irradiating light beam distortion, and sharpens focusing. Various physical and chemical actions, such as compression, stretching, dehydration, coagulation, and impregnation by biocompatible chemical agents are widely described in the literature as tools for controlling of tissue optical properties. As a major technology, the optical immersion method for use as exogenous optical clearing agents (OCAs) is discussed. Some important applications of the tissue immersion technique are described, such as glucose sensing, improvement of image contrast and imaging depth, laser radiation delivery, precision tissue laser photodisruption, and so on.

7.2
Light–Tissue Interaction

Light propagation within a tissue depends on the optical properties of its components: cells, cell organelles, and various fiber structures. Typically, the optical properties of tissue are characterized by the absorption and scattering coefficients, which are equal to the average number of absorption and scattering events per unit path length of a photon traveling in the tissue, and the anisotropy factor, which represents the average cosine of the scattering angles. The size, shape, and density of tissue structures, their refractive index relative to the tissue ground substance, and the polarization states of the incident light all play important roles in the propagation

Laser Imaging and Manipulation in Cell Biology. Edited by Francesco S. Pavone

ISBN: 978-3-527-40929-7

of light in tissues [1–3]. The sizes of cells and tissue structure elements vary from a few tenths of nanometers to hundreds of micrometers.

In fibrous tissues (cornea, sclera, skin dermis, dura mater, muscle, myocardium, tendon, cartilage, vessel wall, etc.) and tissues composed mostly of microfibrils and/or microtubules, typical diameters of the cylindrical structural elements are 10–400 nm. Their length is in a range from 10–25 μm to a few millimeters [3]. The size distribution of the scattering particles may be essentially monodispersive (e.g., transparent eye cornea stroma) or quite broad, as in a turbid eye sclera [1, 2].

The collagen fibrils of fibrous tissues are arranged in individual bundles in a parallel fashion. Moreover, within each bundle the groups of fibril are separated from each other by the large empty lacunae distributed randomly in space. Collagen bundles have a wide range of widths and thicknesses. The bundles are much longer than their 0.5–8-μm diameters [4]. These ribbon-like structures are multiply cross-linked. They cross each other in all directions but remain parallel to the surface [3].

The interstitial fluid constitutes a clear, colorless liquid containing proteins, proteoglycans, glycoproteins, and hyaluronic acid. Owing to their glycosaminoglycan chains, these molecules concentrate negative charges. They are highly hydrophilic and have a propensity to attract ions, creating an osmotic imbalance that results in the glycosaminoglycan absorbing water from surrounding areas [5].

The hollow organs of the body are lined with a thin, highly cellular surface layer of epithelial tissue (oral region, maxillary sinuses, stomach, etc.), which is supported by underlying, relatively acellular connective tissue. In healthy tissue, the epithelium often consists of a single well-organized layer of cells with an *en face* diameter of 10–20 μm and height of 25 μm. In dysplastic epithelium, cells proliferate and their nuclei enlarge [3].

The outermost cellular layer of skin is epidermis, which consists of stratum corneum (SC) (mostly dead cells) and four layers of living cells. SC is a lipid-protein biphasic structure that is only 10–20 μm thick on most surfaces of the body. Owing to cell membrane keratinization, tight packing of cells, and lipid bridges between them, SC is a dense medium with poor penetration for foreign molecules [6]. Living epidermis (100 μm thick) contains most of the skin pigmentation, mainly melanin, which is produced in the melanocytes [7]. Large melanin particles, such as melanosomes (>300 nm in diameter), exhibit mainly forward scattering due to their high refractive index and relatively large size (up to 1–2 μm). In contrast, melanin dust, whose particles are small (<30 nm in diameter), provides the isotropy in the scattering profile; the optical properties of the melanin particles (30–300 nm in diameter) may be predicted by the Mie theory [8].

There are a wide variety of structures within cells that determine tissue light scattering [1–3]. Cell nuclei are on the order of 5–10 μm in diameter, mitochondria, lysosomes, and peroxisomes have dimensions of 1–2 μm, ribosomes are on the order of 20 nm in diameter, and structures within various organelles can have dimensions of up to a few hundred nanometers [3].

The absorption spectrum depends on the type of predominant absorption centers and the water content in tissues. Absorption for most tissues in the visible region is insignificant, except for the absorption bands of blood hemoglobin and some other

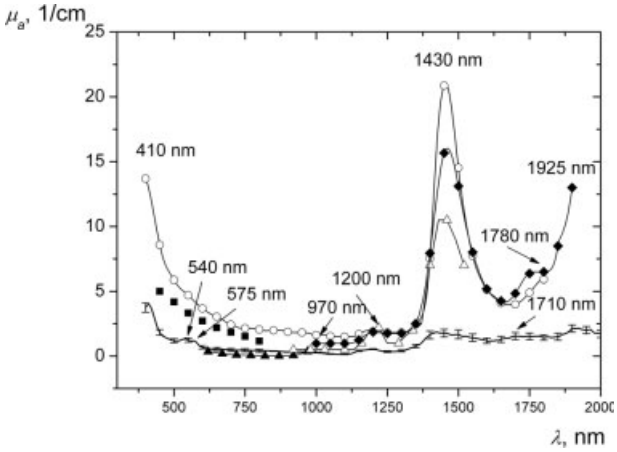

Figure 7.1 Wavelength dependence of the absorption coefficient (μ_a) of human skin *in vitro*. The solid line corresponds to the averaged experimental data, presented in Reference [9], and the vertical lines show the standard deviation values. Data taken from various sources: filled squares [10], open circles [11], filled triangles [12], open triangles [13], and filled diamonds [14].

chromophores [7]. The absorption bands of protein molecules are mainly in the near-UV region. Absorption in the IR region is essentially defined by water contained in tissues. Absolute values of absorption coefficients for typical tissues are in the range 10^{-2}–$10^{4}\,\mathrm{cm}^{-1}$ [3].

Figure 7.1 shows the wavelength dependence of the absorption coefficient of human skin presented by different authors [9–14]. The vertical lines correspond to the values of standard deviation (SD) [9].

In the figure the absorption bands of oxyhemoglobin with maxima at about 410, 540 and 575 nm are observed in the visible spectral range [9, 15]. Absorption of water in this spectral range is negligible [16]. Absorption spectra of most tissues, such as sclera, dura mater, mucosa, adipose tissues, bone, and so on, have a similar form in this spectral range [3, 9, 17–20]. In the NIR spectral range, the main chromophores are water and lipids, which are contained in different tissues in various quantities. In this spectral range, the absorption bands of water in skin with maxima at 970 [21], 1430, and 1925 nm [22] and lipids with maxima at 1710 and 1780 nm [23] are seen. At the same time, a low-intensity lipid absorption band with maximum at 930 nm [21] is not observed. The absorption band with maximum at about 1200 nm is the combination of the absorption bands of water (maximum at 1197 nm [22]) and lipids (maximum at 1212 nm [24]). The discrepancies between results obtained by different authors can be connected with the natural variability of tissue properties and the methods used for tissue preparation and storage.

Most tissues are turbid media showing a strong scattering and much less absorption (up to two orders less than scattering in the visible and NIR ranges). Moreover, tissues are rather thick. Therefore, multiple scattering is a specific feature of a wide class of tissues [1–3].

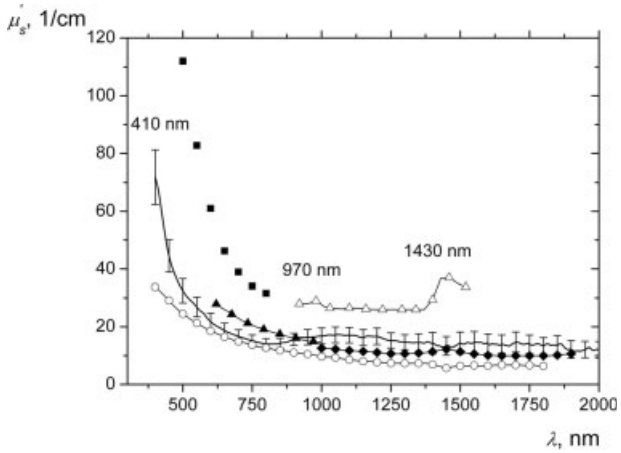

Figure 7.2 Spectral dependence of reduced scattering coefficient (μ_s') of human skin *in vitro*. The solid line corresponds to the averaged experimental data presented in Reference [9] and the vertical lines show the standard deviations. Data taken from various sources: filled squares [10], open circles [11], filled triangles [12], open triangles [13], and filled diamonds [14].

Utilizing the interaction of light with biological tissues for practical purposes depends on an understanding of the properties of two large classes of biological media. One consists of weakly scattering (transparent) tissues like cornea and the crystalline lens of eye. The other class includes strongly scattering (opaque or turbid) tissues like skin, brain, vessel wall, and eye sclera [25, 26].

Figure 7.2 presents spectral dependences of the scattering properties (shown as reduced scattering coefficient $\left[\mu_s' = \mu_s(1-g)\right]$, where μ_s is the scattering coefficient, and g is the anisotropy factor of scattering) of human skin tissue [9–14]. The anisotropy factor is usually fixed as 0.9, since this value is typical for many tissues in the visible and NIR spectral ranges [3]. The vertical lines indicate the SD values.

Figure 7.2 shows that the reduced scattering coefficient of tissues decreases with increasing wavelength in the range 400–1400 nm. However, in the spectral range from about 1400 to 2000 nm the reduced scattering coefficient can have peaks corresponding to the strong absorpation bands of water [13]. The deviation of the spectrum of the reduced scattering coefficient from a monotonic dependence can be explained by an increase of the real part of the complex refractive index of the tissue scatterers due to anomalous light dispersion. In the range of strong absorption bands, the effect produces a significant decrease of the anisotropy factor, which leads to an increase of the reduced scattering coefficient [9].

Many tissues – such as eye cornea, sclera, tendon, and cartilage, which are classified as fibrous tissues, and other structured tissues such as retina, tooth enamel, and dentin – show a wide variety of polarization properties: linear birefringence, optical activity, and linear dichroism (diattenuation). These properties are

primarily defined by the tissue structure – anisotropy of form – or by the intrinsic anisotropic character of the tissue components or metabolic molecules – anisotropy of material. A large variety of tissues, such as eye cornea, tendon, cartilage, eye sclera, dura mater, testis, muscle, nerve, retina, bone, teeth, myelin, and so on, exhibit birefringence. All of these tissues contain uniaxial and/or biaxial birefringent structures [26].

Often the vector nature of light transport in scattering media, such as tissues, is ignored because of its rapid depolarization during propagation in a randomly inhomogeneous medium. However, in certain tissues (transparent eye tissues, cellular monolayers, mucous membrane, superficial skin layers, etc.), the degree of polarization of the transmitted or reflected light is measurable even when the tissue has a considerable thickness [3].

Luminescence is one of the fundamental mechanisms of interaction between light and biological objects. Luminescence is subdivided into fluorescence, corresponding to an allowed optical transition with a rather high quantum yield and a short (nanosecond) lifetime, and phosphorescence, corresponding to a "forbidden" transition with low quantum yield and long decay times in the microsecond–millisecond range [27, 28].

Fluorescence arises upon light absorption and is related to an electronic transition from the excited state to the ground state of a molecule. After excitation of biological objects by ultraviolet light ($\lambda \leq 370$ nm), fluorescence of proteins as well as of nucleic acids can be observed. Autofluorescence of proteins is related to the amino acids tryptophan, tyrosine, and phenylalanine with absorption maxima at 280, 275, and 257 nm, respectively, and emission maxima between 280 nm (phenylalanine) and 350 nm (tryptophan) [3, 27–29]. The protein spectrum is usually dominated by tryptophan. Fluorescence from collagen or elastin is excited between 400 and 600 nm with maxima around 400, 430, and 460 nm. Fluorescence of collagen and elastin can be used to distinguish various types of tissues, for example, epithelial and connective tissues [28–31].

The reduced form of coenzyme nicotinamide adenine dinucleotide (NADH) is excited selectively in the wavelength range 330–370 nm. NADH is most concentrated within mitochondria, where it is oxidized within the respiratory chain located within the inner mitochondrial membrane, and its fluorescence is an appropriate parameter for detection of ischemic or neoplastic tissues [28, 31]. Flavin mononucleotide (FMN) and dinucleotide (FAD) with excitation maxima around 380 and 450 nm have been reported to contribute to intrinsic cellular fluorescence [28].

Porphyrin molecules, for example, protoporphyrin, coproporphyrin, uroporphyrin, or hematoporphyrin, occur within the pathway of biosynthesis of hemoglobin, myoglobin, and cytochromes. Abnormalities in heme synthesis, occurring in the cases of porphyries and some hemolytic diseases, may enhance the porphyrin level within tissues considerably. Several bacteria, for example, *Propionibacterium acnes*, or bacteria within dental plaque (biofilm), such as *Porphyromonas gingivalis*, *Provotella intermedia*, and *Prevotella nigrescens*, accumulate considerable amounts of protoporphyrin [32, 33]. Therefore, acne or oral and tooth lesion detection based on measurements of intrinsic fluorescence appears to be a promising method [3].

Fluorescence spectra often give detailed information on fluorescent molecules, their conformation, binding sites, and interaction within cells and tissues. At present, various exogenous fluorescing dyes can be applied to probe cell anatomy and cell physiology [34, 35]. In humans, one such dye as indocyanine green, which is used as a diagnostic aid for blood volume determination, cardiac output, and hepatic function [36].

The depth penetration of light into a biological tissue is an important parameter for many methods of optical biomedical diagnostic and also for the correct determination of the irradiation dose in photothermal and photodynamic therapy of various diseases [1–3].

The optical transparency of tissues is maximal in the near-infrared (NIR) region, which is due to the absence, in this spectral range, of strong intrinsic chromophores that would absorb radiation in living tissues [9]. However, these tissues are characterized by rather strong scattering of NIR radiation, which prevents the attainment of clear images of localized inhomogeneities arising due to various pathologies, for example, tumor formation or the growth of microvessels.

The light penetration depth (δ) can be estimated with the relation [37]:

$$\delta = 1/\sqrt{3\mu_a\left(\mu_a + \mu_s'\right)}$$

where μ_a is the absorption coefficient and μ_s' is reduced scattering coefficient.

Table 7.1 shows the values of light penetration depth at some wavelengths used in diagnostics and photodynamic therapy for different tissues.

7.3 Tissue Clearing

In general, the scattering coefficient (μ_s) and scattering anisotropy factor (g) of a tissue depend on the refractive index mismatch between cellular tissue components: cell membrane, cytoplasm, cell nucleus, cell organelles, melanin granules, and the extracellular fluid. For fibrous (connective) tissue (eye scleral stroma, corneal stroma, skin dermis, cerebral membrane, muscle, vessel wall noncellular matrix, female breast fibrous component, cartilage, tendon, etc.) index mismatch of interstitial medium and long strands of scleroprotein (collagen-, elastin-, or reticulin-forming fibers) is important [26].

The nucleus and the cytoplasmic organelles in mammalian cells that contain similar concentrations of proteins and nucleic acids, such as the mitochondria and the ribosomes, have refractive indices that fall within a relative narrow range (1.38–1.41) [40]. The measured index for the nuclei is $n_{nc} = 1.39$ [41]. The ground matter index is usually taken as $n_0 = 1.35$–1.37. The scattering particles themselves (organelles, protein fibrils, membranes, protein globules) exhibit a higher density of proteins and lipids than the ground substance and, thus, a greater index of refraction ($n_s = 1.39$–1.47) [26]. The refractive index of the connective-tissue fibers is about 1.47, which corresponds to approximately 55% hydration of collagen, its main component, and the refractive index of the interstitial liquid is 1.35 [3].

Table 7.1 Light penetration depth (mm) for different tissues obtained at different wavelengths on the basis of data presented in References [9,17,18,20,38,39].

Tissue	Wavelengths (nm)								Reference
	532	633	675	694	780	835	930	1064	
Human skin	0.9 ± 0.1	1.7 ± 0.1	1.8 ± 0.1	1.9 ± 0.1	2.2 ± 0.1	2.3 ± 0.1	2.5 ± 0.1	3.4 ± 0.12	[9]
Human sclera	0.75 ± 0.05	1.34 ± 0.1	1.55 ± 0.15	1.64 ± 0.2	1.99 ± 0.2	2.18 ± 0.2	1.91 ± 0.1	2.56 ± 0.3	[38]
Human dura mater	1.2 ± 0.1	1.7 ± 0.1	$1,7 \pm 0.1$	1.7 ± 0.1					[20]
Human maxillary sinuses mucous	1.3 ± 0.1	1.4 ± 0.1	1.5 ± 0.1	1.5 ± 0.1	1.6 ± 0.1	1.6 ± 0.1	1.7 ± 0.1	1.8 ± 0.1	[9]
Human stomach wall mucous	0.7 ± 0.1	1.5 ± 0.1	1.7 ± 0.1	1.7 ± 0.1	1.8 ± 0.1	1.9 ± 0.1	1.8 ± 0.1	1.8 ± 0.1	[17]
Liver		1.2 ± 0.13	1.69 ± 0.16		2.91 ± 0.3		3.68 ± 0.35		[39]
Muscle		1.47 ± 0.1	1.63 ± 0.1		3.46 ± 0.23		3.72 ± 0.29		[39]
Cranial bone	1.25 ± 0.1	1.4 ± 0.1	1.47 ± 0.1	1.5 ± 0.1	1.56 ± 0.1	1.6 ± 0.1	1.7 ± 0.1	1.8 ± 0.1	[18]

The living tissue allows one to control its optical (scattering) properties using various physical and chemical actions. Turbidity of a dispersive physical system can be effectively controlled by providing matching of refractive indices of the scatterers and the ground material. This is a so-called optical immersion technique. It is also possible to control optical properties of a disperse system by the change of its packing parameter and/or scatterer sizing.

7.3.1
Compression and Stretching

It is possible to increase significantly transmission through a soft tissue by squeezing (compressing) or stretching it [42]. The optical clarity of living tissue is due to its optical homogeneity, which is achieved through the removal of blood and interstitial liquid (water) from the compressed site. This results in a higher refractive index of the ground matter, whose value becomes close to that of scatterers (cell membrane, muscle, or collagen fibers). More close packing of tissue components at compression makes the tissue a less chaotic, more organized system, which may give less scattering due to cooperative (interference) effects. Indeed, the absence of blood in the compressed area also contributes to altered tissue absorption and refraction properties. Certain mechanisms underlying the effects of optical clearing and changing of light reflection by tissues at compression and stretching have been proposed in References [20, 43].

Several laser surgery, therapy, and diagnostic technologies include tissue compression and stretching for better transportation of the laser beam to underlying layers of tissue. The human eye compression technique allows one to perform transscleral laser coagulation of the ciliary body and retina/choroids [44].

7.3.2
Dehydration and Coagulation

Evidently, the loss of water by tissue seriously influences its optical properties. Under *in vitro* conditions spontaneous water evaporation from tissue, tissue sample heating at non-coagulating temperature, or its freezing in a refrigerator cause tissue to lose water. Typically, in the visible and NIR, far from water absorption bands, the absorption coefficient increases by a few dozen percentage points and the scattering coefficient by a few percentage points due to more close packing of tissue components caused by its shrinkage. However, the overall optical transmittance of a tissue sample increases due to a decrease of its thickness at dehydration [45]. Specifically, near the strong water absorption bands the tissue absorption coefficient decreases, due to a lower concentration of water, despite the higher density of tissue at its dehydration.

One of the major reasons for tissue dehydration *in vivo* is the action of endogenous or exogenous osmotic liquids. Dehydration induced by osmotic stimuli such as optical clearing agents (OCAs) appears to be a primary mechanism of optical clearing in collagenous and cellular tissues, whereas dehydration induces the intrinsic matching effect [46–48].

The fluid space between fibrils and organelles is filled by water and suspended salts and proteins. As water is removed from the intrafibrillar or intracellular space, soluble components of interstitial fluid become more concentrated and the refractive index increases. The resulting intrinsic refractive index matching between fibrils or organelles and their surrounding media, as well as the density of packing and particle ordering, may significantly contribute to optical clearing [46–50].

Since tissue dehydration is associated with diffusion of water from the tissue to external volume, the experimentally measured kinetics of the change of dehydration degree can be described on the basis of the equation describing diffusion through a permeable membrane. To estimate the degree of tissue dehydration under drying by hot air and/or by action of hyperosmotic agent, the following equation can be used, which describes the flow of substance from a small volume with nonzero concentration into a reservoir with zero concentration [51, 52]:

$$H_D(t) = \frac{M(t=0) - M_0}{M(t=0)} [1 - \exp(-t/\tau_D)] \tag{7.1}$$

where

M is a mass of the tissue (skin) sample (g),
M_0 corresponds to the permanent mass of the sample (i.e., dry mass) (g),
τ_D is a time constant that characterizes the rate of dehydration (s)
t is the time of dehydration (s).

The parameter M_0 includes the mass of collagen, elastin, and other components of tissue after its total dehydration, bound water, and possibility residual free water. The difference between initial and permanent mass of the sample $[M(t=0) - M_0]$ shows the amount of water escaped from tissue due to dehydration [48].

Skin dehydration kinetics induced by the stimuli of evaporation and application of OCAs is demonstrated in Figure 7.3. To enhance skin membrane permeability the SC of the samples was perforated [48, 53].

Figure 7.3 clearly shows that the degree of resulting dehydration under the influence of the osmotic agents is lower than that of air. This effect could be related to the fact that, on the one hand, glycerol, as a hyperosmotic agent, stimulates diffusion flow of free water from tissue to surrounding OCAs solution, while, on the other hand, it prevents total dehydration of tissue due to holding water inside. Glycerol is extremely hygroscopic and when left to equilibrate in a moist environment it will attract water until it reaches a level of 55% (w/w), meaning that each molecule of glycerol attracts about six molecules of water. Small hygroscopic molecules penetrate the SC where they subsequently act as a humectant. Glycols and other polyhydroxy molecules like propylene glycol, butylene glycol, glucose, saccharose, and sorbitol also work via this mechanism [54]. As glycerol viscosity decreases, it penetrates into tissue and binds molecules of water in deeper layers. In contrast, for skin dehydration in air, free water evaporates from tissue almost completely [48, 50].

Long-pulsed laser heating induces reversible and irreversible changes in the optical properties of tissue [45]. In general, the total transmittance decreases and the diffuse reflectance increases, showing nonlinear behavior during pulsed laser

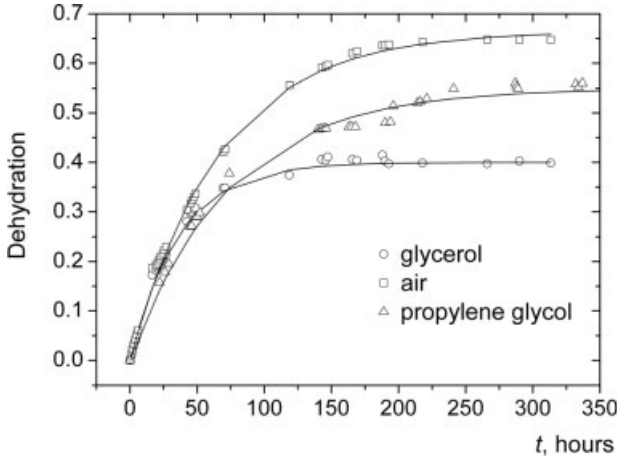

Figure 7.3 Kinetics of dehydration degree of human skin samples with damaged stratum corneum: (open squares) dehydration in air [48], (open circles) dehydration by glycerol [48], and (open triangles) dehydration by propylene glycol [53]. Symbols present experimental data, solid lines correspond to approximated dependence.

heating. Many types of tissues slowly coagulated (from 10 min to 2 h) in a hot water or saline bath (70–85 °C) exhibit an increase of their scattering and absorption coefficients [46].

7.3.3
Optical Immersion

The optical immersion technique is based on the impregnation of a tissue by a biocompatible chemical agent, which may have some hyperosmotic properties. OCAs used frequently are glucose, dextrose, fructose, glycerol, mannitol, sorbitol, propylene glycol, poly(propylene glycol), poly(ethylene glycol), 1,3-butanediol, 1,4-butanediol, and their combinations, X-ray contrasting agents (verografin, trazograph, and hypaque), and so on [20, 47–49, 52, 53, 55–63].

There are a few main mechanisms of light scattering reduction induced by an OCA [47–49, 52–64]: (i) dehydration of tissue constituents, (ii) partial replacement of the interstitial fluid by the immersion substance, and (iii) structural modification or dissociation of collagen.

The first mechanism is characteristic only for highly hyperosmotic agents. For fibrous tissue similar to sclera, dura mater, dermis, and so on, while the second mechanism is preferable for all tested chemical agents because their molecule sizes are much less than the mean cross-section of interfibrillar space, which is about 185 nm, when the diameter of the biggest molecule of PEG (20 000) is less than 5 nm [3]. Both the first and second processes mostly cause matching of the refractive indices of the tissue scatterers (cell compartments, collagen, and elastin fibers) and the cytoplasm and/or interstitial fluid.

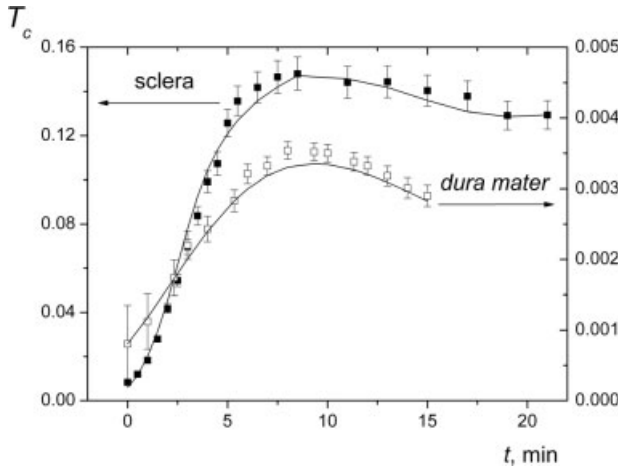

Figure 7.4 Time-dependent collimated transmittance of the human sclera and dura mater samples measured at wavelength 700nm concurrently with administration of 40%-glucose solution. Symbols correspond to the experimental data measured by a multichannel fiber-optic spectrometer LESA-6med (BioSpec, Russia). Error bars show the SD values. Solid lines correspond to the data calculated using the model presented in References [52, 63].

Figure 7.4 illustrates the kinetics of collimated transmittance of both human sclera and dura mater samples measured at wavelength 700nm concurrently with administration of aqueous 40%-glucose solution [52, 63].

It is easily seen that the untreated sclera and dura mater are poorly transparent media for visible light. Glucose administration makes these tissues highly transparent; the collimated transmittance increases 2.5–3-fold. The figure shows that the clearing process has at least two stages. At the beginning of the process the increase of the transmittance is seen, which is followed by saturation and even the decrease of the transmittance. Two major processes could take place. One of them is diffusion of glucose inside tissue and another is tissue dehydration caused by osmotic properties of the agent. In general, both processes lead to matching of refractive indices of the scatterers and the interstitial fluid that causes the decrease of tissue scattering and, therefore, the increase of the collimated transmittance. Dehydration also leads to the additional increase of optical transmission due to a decrease of tissue thickness (shrinkage) and a corresponding scatterer ordering process due to increase of particle volume fraction. However, the increase of scatterer volume fraction may also cause some competitive increase of scattering coefficient due to a random packing process (growth of particle density) that partly compensates the immersion effect. The saturation of optical clearing kinetic curves (Figure 7.4) can be explained as the saturation of glucose and water diffusion processes. Such kinetics of collimated transmission of tissue is featured not only for glucose but also for mannitol and other OCAs [52]. Some darkening at the late time period may be attributed to a few causes, such as the above-mentioned particle density growth and interaction of modified

interstitial fluid (containing OCA and less water) with hydrated collagenous fibrils [46].

Structural modification also leads to tissue shrinkage, that is, to the near-order spatial correlation of scatterers and, as a result, the increased constructive interference of the elementary scattered fields in the forward direction and destructive interference in the perpendicular direction of the incident light, which may significantly increase tissue transmittance even at some refractive-index mismatch [46]. For some tissues and for the non-optimized pH of clearing agents, tissue swelling may take place that could be considered as a competitive process in providing tissue optical clearing [46, 51].

The optical clearing process in collagen-based tissues may involve a change in the supramolecular structure. Reversible solubility of collagen in sugars and sugar alcohols may take place [64]. It was demonstrated that glycerol treatment induces swelling of interfibrillar space and dissociation of collagen fibrils into microfibrils (loss of characteristic bonding in some areas). Agent-induced destabilization of collagen structures may lead to additional reduction of optical scattering in tissue due to a smaller size of the main scatterers [64].

The refractive index matching is manifested in the reduction of the scattering coefficient ($\mu_s \to 0$) and increase of single scattering directness ($g \to 1$). For fibrous tissues like skin dermis, eye sclera, dura mater, tendon, and so on, μ_s reduction can be very high [46, 49, 52, 55, 58–60]. For hematous tissue, such as the liver, its impregnation by solutes with different osmolarity also leads to refractive index matching and reduction of scattering coefficient, but the effect is not so pronounced as for fibrous tissues due to cells changing size as a result of osmotic stress [65].

For a two-component model, the mean refractive index of a tissue ($\bar{n}$) is defined by the refractive indices of its scattering centers material (n_s) and ground matter (n_0) as $\bar{n} = f_s n_s + (1 - f_s) n_0$, where f_s is the time-dependent volume fraction of the scatterers in a tissue [66]. The $n_s/n_0 \equiv m$ ratio determines the scattering coefficient. For example, the expression for the scattering coefficient, derived for a system of non-interacting thin cylinders with the number of fibrils per unit area (ϱ_s) has a form [8, 58]:

$$\mu_s \cong \varrho_s \left(\frac{\pi^5 a^4 n_0^3}{\lambda_0^3} \right) (m^2 - 1)^2 \left[1 + \frac{2}{(m^2 + 1)^2} \right] \tag{7.2}$$

where

$\varrho_s = f_{cyl}/\pi a^2$, where f_{cyl} is the surface fraction of the cylinders' faces,
a is the cylinder radius,
λ_0 is the wavelength in vacuum.

As a first approximation it is reasonable to assume that the radii of the scatterers (fibrils) and their density cannot be significantly changed by chemicals (no tissue swelling or shrinkage take place), the absolute changes of n_0 is not very high, and variations in μ_s are caused only by the change in the refractive index of the interstitial (interfibrillar) space with respect to the refractive index of the scatterers. Then, accounting for the fact that for most tissues $m \approx 1$, the ratio of the scattering

coefficients at a particular wavelength as a function of refractive index ratio *(m)* can be written in the form [58]:

$$\mu_{s2} \cong \mu_{s1}\left(\frac{m_2-1}{m_1-1}\right)^2 \tag{7.3}$$

Indeed, this relation describes the change in tissue scattering properties due to refractive index matching or mismatching caused by changes of refractive indices of the scatterers or the background or both. Owing to square dependence, the sensitivity to indices matching is very high; for instance, only a 5% increase in the refractive index of the ground matter ($n_0 = 1.35 \rightarrow 1.42$), when that of the scattering centers is $n_s = 1.47$, will cause a sevenfold decrease of μ_s. In the limit of equal refractive indices for non-absorbing particles and background material, $m = 1$ and $\mu_s \rightarrow 0$ [46].

Notably, for hyperosmotic agents, fluid transport within tissue is more complicated because there are at least two interacting fluxes, so the model for describing of these processes should be more complicated and should include monitoring of additional measurement parameters, such as the refractive index of the chemical agent, tissue weight and/or thickness, and osmotic pressure in a process of tissue clearing [58].

Measured values of osmotic pressure for trazograph-60 and trazograph-76 were 4.3 and 7.1 MPa, respectively. For untreated sclera, the osmotic pressure was 0.74 MPa, and increased after administration of trazograph-60 for 30 min – up to 5.02 MPa [67]. On the one hand, the osmotic pressure causes the generation of flows and their intensities but, on the other hand, rather strong osmotic pressure may destroy tissue structure. A direct histological study has shown that there are no serious irreversible changes in the cellular and fibrous structure of the human sclera for a rather long (about 30 min) period of OCA administration [67].

Figure 7.5 presents the change in spectra of dura mater optical parameters under the action of aqueous mannitol solution (0.16 g ml^{-1}). Figures 7.5a and b show that administration of the aqueous solution of mannitol into the dura mater changes both the scattering and the absorption characteristics of this biological tissue. During clearing, the scattering decreases, on average, 1.5–2-fold in the wavelength range under study. The absorption coefficient decreases mainly in the ranges of the absorption bands of blood (Figure 7.5a). Within the Soret band, the absorption decreases, on average, 1.5-fold, and, in the range 500–600 nm, it decreases 1.2-fold [20].

This decrease in absorption is explained by a decrease in the probability of absorption of photons in an elementary volume of the tissue due to a decrease in the mean free path of photon migration within the tissue during its clearing. In addition, mannitol penetrates the vessel walls and affects the optical properties of the blood. This influence leads to a partial matching between the refractive indices of the red blood cells (erythrocytes) and the blood plasma and to a decrease in the imaginary part of the complex refractive index of the erythrocytes. This decreases both the absorption and the scattering characteristics of the blood [20].

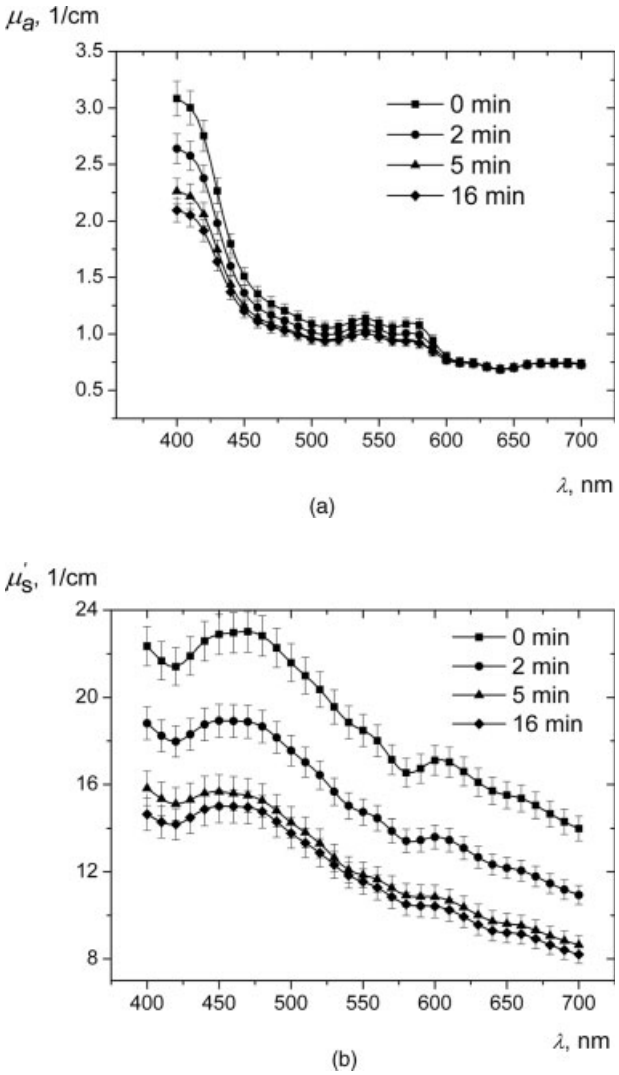

Figure 7.5 Spectra of absorption (a) and reduced scattering (b) coefficients of human dura mater sample during optical clearing under action of aqueous mannitol solution (0.16 g ml^{-1}) [20]. Bars correspond to standard deviations.

Therefore, upon penetration of OCA into the interstitial fluid of the tissue, the refractive index of the interstitial fluid increases, whereas both the real and the imaginary parts of the relative refractive indices of the scattering (collagen fibrils) and absorption (erythrocytes) centers of the tissue decrease. As a result, the scattering spectrum of the tissue in the ranges of the blood absorption bands is transformed in the course of time in such a way that the valleys become shallow and the spectral

dependence of the transport scattering coefficient becomes more monotonic (Figure 7.5b) [20].

In a living tissue the relative refractive index is a function of tissue physiological or pathological state. Depending on the specificity of tissue state, the refractive index of the scatterers and/or the background may be changed (increase or decrease) and, therefore, light scattering may correspondingly increase or decrease [3, 46].

It is known that for *in vivo* application of the designed optical immersion technology additional factors such as metabolic reaction of living tissue on clearing agent application, the specificity of tissue functioning, and its physiological temperature can significantly change the kinetic characteristics and magnitude of the clearing effect [8, 49, 55, 60, 68].

Figure 7.6 presents the *in vivo* reflectance spectra of rabbit eye sclera and human skin measured at 700 nm at different time intervals after administration of a 40%-glucose solution [60, 68].

The kinetics of the polarization properties of the tissue sample at immersion can be easily observed using an optical scheme with a white light source and a tissue sample placed between two parallel or crossed polarizers. At a reduction of scattering, the degree of linearly polarized light propagating in fibrous tissue improves [26, 69].

As the tissue is immersed, the number of scattering events decreases and the residual polarization degree of transmitted linearly polarized light increases. As a result, the kinetics of the average transmittance and polarization degree of the tissue are similar. OCA-induced optical clearing leads to increasing depolarization length [69].

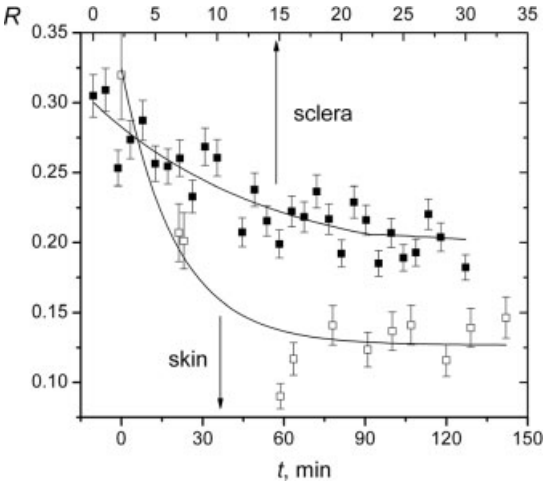

Figure 7.6 *In vivo* reflectance spectra of rabbit eye sclera and human skin measured at 700 nm at different time intervals after administration of 40%-glucose solution [60, 68]. Symbols and solid curves correspond to experimental data and their approximation, respectively.

7.4
Enhancers of Diffusion

7.4.1
Diffusion through Membranes

Several laser surgery, therapy, and noninvasive diagnostic technologies may benefit significantly from a reversible skin scattering reduction. However, slow diffusion of OCAs through a human skin barrier makes practical application of the optical immersion effect difficult.

It is well known that diffusion of aqueous solutions of substances through SC barrier is hindered. The SC is between 100 and 200 μm thick. It contains the corneocytes or horny cells, which are closely packed flat non-nucleated cells, approximately 40 μm in diameter and 0.5 μm thick. Polar structures such as corneodesmosomes contribute to SC cohesion [6]. Corneocytes are embedded in a lipid bilayer matrix. The intercellular lipids are required for a competent skin barrier and form the only continuous domain in SC [6]. Appendages such as hair follicles and sweat glands cover approximately 0.1% of the total skin surface [70].

Thus, the heterogeneous nature of SC provides some possible pathways for solute transport: appendageal, transcellular (through both corneocytes and lipid bridges), and intercellular (through the lipid phase only) [70]. Lipophilic and polar permeants are transported by the lipoidal and pore pathway of SC, respectively [71].

The pathway for water diffusion across SC has been calculated to be 50-fold longer than the thickness of SC. This suggests that permeation follows a tortuous path through the intercellular lipid matrix [6]. Penetration of compounds into the corneocytes also takes place since immersion of skin leads to swelling of the corneocytes connected with the entry of water [6]. Thus, the structure and composition of SC provides the diffusion coefficient, which is 10^3-fold less than that observed for cellular membranes [70]. The diffusion coefficient of water through SC varies in the range $2.5–8.34 \times 10^{-10}\,\mathrm{cm^2\,s^{-1}}$ depending on the humidity of SC [71].

Diffusion of OCA through tissue layer or cell wall can be presented as diffusion of a dissolved substance through a membrane [58]. Based on Fick's first law, which limits the flux of matter (J, $\mathrm{mol\,s^{-1}\,cm^{-2}}$) to the gradient of its concentration:

$$J = -D\frac{\mathrm{d}c}{\mathrm{d}x} \tag{7.4}$$

For stationary transport of matter through a thin membrane, we have [72]:

$$J = P(c_1 - c_2), \tag{7.5}$$

where

$P = D/l$ is the coefficient of permeability, where D is the diffusion coefficient and l is the thickness of a membrane,

c_1 and c_2 are the concentrations of molecules in two spaces separated by a membrane.

Permeability of molecules across a membrane can be expressed as $P = KP_m$, where K is the partition coefficient and P_m is the permeability inside a membrane. The diffusion coefficient is a measure of the rate of entry into the cytoplasm (in the case of diffusion into a cell) or into tissue behind membrane (e.g., SC) depending on the molecular weight or size of a molecule and viscosity of a medium (e.g., the behavior of spherical molecules obeys the Stokes–Einstein law: $D = RT/6N\pi\eta r$, where N is the Avogadro constant, η is the viscosity of a medium, and r is the radius of a molecule). The term K is a measure of the solubility of the substance in lipids. A low value of K describes a molecule like water that is not soluble in lipid. This means that water, being a highly diffusive molecule, does not penetrate through lipid membranes because of its small solubility. For oils solubility is high, but diffusivity (due to high viscosity) could be low. Water and small hydrophilic molecules can penetrate only through hydrophilic pores in the membrane [72].

Owing to its fibrous structure a tissue can be presented as a porous material, which leads to modification of the chemical agent diffusion coefficient [3]:

$$D = \frac{D_i}{p} \tag{7.6}$$

Here, D_i is the chemical agent diffusion coefficient within the interstitial fluid and p is the porosity coefficient defined as:

$$p = \frac{V - V_C}{V} \tag{7.7}$$

where V is the volume of the tissue sample, and V_C is the volume of collagen fibers.

In general, biological membranes are permeable for both water and dissolved substances, but the degree of permeability for them can be quite different.

The intrinsic routes and mechanisms for transport of OCAs across the human SC and enhancement of a molecule's transport by both physical and chemical enhancers of permeation are problems under investigation.

7.4.2
Chemical Agents

As enhancers of OCA diffusivity through SC, ethanol, propylene glycol, dimethyl sulfoxide (DMSO), linoleic and oleic acids, azone, and thiazone are used [73–77].

Sometimes DMSO alone is used as the OCA due to its own extremely high permeability (as a polar aprotic solvent of SC lipids) and its high index of refraction [78].

The addition of ethanol to a solution induces a significant increase in the diffusion rate. Ethanol is a solvent known to modify the skin barrier property. The influence of ethanol on the *in vitro* transport behavior of some polar/ionic permeants in hairless mouse skin has been investigated over different ethanol/saline concentrations [73, 74]. At high concentrations (~40%) ethanol greatly enhances pore transport due to bigger pores and/or pore density of the epidermal membrane under alcohol action. This can be explained by altered or additional pore/polar pathways, which may

be formed as a result of a combination of changes in the protein conformation, reorganization within the lipid polar head regions, or lipid extraction [79]. Lipid extraction may take place in conjunction with and/or independently of conformational alterations with protein domains [73].

The solvation of keratin within the SC by competition with water for the hydrogen bond binding sites and the intercalation in the polar head-groups of the lipid bilayers by propylene glycol are postulated as mechanisms for the penetration enhancing effects of propylene glycol [80]. Mixtures of different OCAs with propylene glycol increase the effectiveness of the optical clearing effect, and the clearing effect induced by propylene glycol itself is worse than that by the OCAs [78].

For thiazone and azone, a possible mechanism is an increase of fluidity of the hydrophobic SC regions and a corresponding reduction of the permeation resistance of the horny layer against drug substances [76, 77].

7.4.3
Physical Methods

Physical methods for transdermal agent delivery have two features in comparison with chemical enhancers: (i) interaction between enhancer and the agents being delivered is absent and (ii) they reduce the risk of additional skin irritation [81]. To reduce the barrier function of skin epidermis, physical methods such as tape stripping [82], microdermabrasion [83], low intensive and high intensive laser irradiation of skin surface [84, 85], iontophoresis [86], ultrasound [87] and photomechanical (shock) waves [81], needle-free injection [88], photothermal and mechanical microperforation [89, 90], or microdamaging of epidermis [91] have been proposed.

The method of tape stripping is the removal of thin strips from the skin surface using "tesa" film. The tapes are pressed onto the skin using a roller and removed with one quick movement, as described in Reference [82]. A skin strip is 3–5 μm thick.

The microdermabrasion system of aspiration–compression uses aluminium oxide crystals, which are fired from the compression system via a nozzle at a pressure of 3 bar. The hand-piece held in contact with the skin for some seconds [83].

Reference [84] utilized a Q-switched Nd:YAG laser (1064 nm) with low intensive (fluence 0.4, 0.5, and 0.6 J cm^2) irradiation together with anhydrous glycerol application to treat rat skin. The experiments showed that laser irradiation together with glycerol can significantly enhance the skin optical clearing effect. Moreover, irradiation combined with treatment of glycerol was demonstrated to be the optimum method at present.

In the method of laser ablation, a NIR laser is used in conjunction with an artificial absorber on the skin surface to create sufficient surface heating, which leads to keratinocyte disruption and skin surface ablation within the selected area-limited site [85].

Iontophoresis results in a reduction of the resistance of the skin to diffusion of ions, but as an enhancer of the flux of uncharged molecules it is a less effective method. Ultrasound and other pressure waves can affect various skin structures and

inner organs due to a large penetration depth, which can be undesirable for specific tasks of OCA delivery.

A method of accelerating the penetration of OCAs due to enhancing the epidermal permeability induced by a fractional skin ablation with creation of a lattice of microzones (islets) of limited photothermal damage or lattice of islets of damage (LID) in the SC has been proposed [89]. LID are created as a result of absorption of a sufficient amount of optical energy by the lattice of microzones. The absorption leads to temperature elevation in the localized zones of interaction in contact with the skin surface. Since the ablation does not affect viable tissue, the long-term effect of fractional SC ablation is the transient deterioration of skin barrier function. This leads to the local increase of OCA penetration. The lattice of optical islets can be formed using various energy sources and delivery optics, including application of lenslet arrays, phase masks, and matrices of exogenous chromophores [48, 89].

The micro-needling method can create microchannels over a large region of skin by applying a mechanic roller. The created microchannels close within hours and the skin returns to its original condition [90]. For microdamaging of SC skin surface, rubbing with a fine 220-grit sandpaper for 2–4 min can be used [91].

For damaged SC, the dehydration of tissue accelerates (Figure 7.3) [48] and OCAs diffuse into the skin more freely; both processes lead to a refractive index matching effect.

Figure 7.7 shows a sample of human skin with a black tattoo before and after application of aqueous glycerol solution during 24 h. The SC of the sample was perforated in advance. Clearly, initially (Figure 7.7a), the tattoo was visualized significantly worse than after treatment (Figure 7.7b). The sample thickness decreased from 0.6 ± 0.05 to 0.5 ± 0.05 mm upon glycerol action [92].

Microperforation of SC, which provides effective impregnation of the upper skin layers over tattoo by an OSA, not only accelerates the skin clearing process but also promotes the increase of absorbed light fraction within the tattoo location [92, 93].

7.5 Diffusion Coefficient Estimation

Knowledge of the coefficients of diffusion and permeability is very important for the development of mathematical models describing interaction between tissues and OCAs, and for evaluation of the agent delivery rate through tissue.

Many biophysical techniques for studying the penetration of various chemicals through living tissue, and for estimation of the both diffusion and permeability coefficients, have been developed over the last 50 years. The methods are based on fluorescence measurements (including fluorescence correlation spectroscopy [94]), spectroscopic [95], Raman [96], and photoacoustic techniques [97], the usage of radioactive labels for detecting matter flux [71, 73, 74], or on the measurements of temporal changes of the scattering properties of a tissue caused by time-dependent refractive index matching [46, 52, 98], including interferometric techniques [99] and optical coherence tomography (OCT) [100, 101]. However, fluorescence techniques

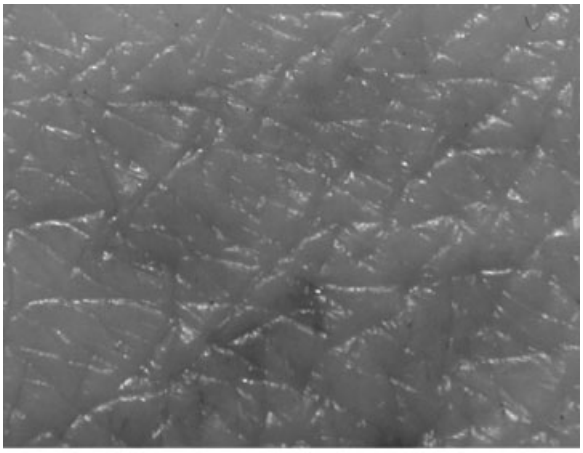

(a)

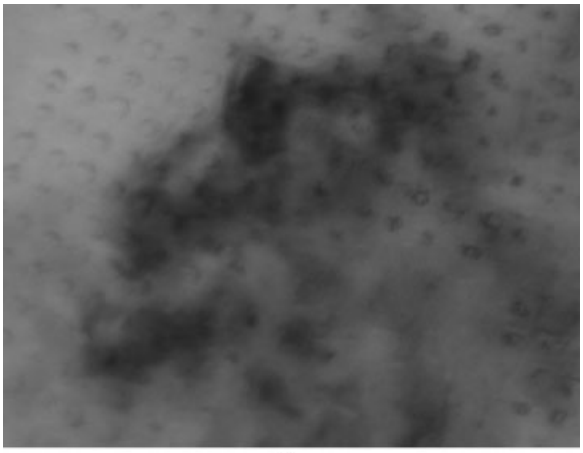

(b)

Figure 7.7 Images of skin surface with black ink tattoo; sample with tattoo before glycerol action (a) and after microperforation of skin surface and glycerol action during 24 h (b) [92].

could not be used for direct measurement of diffusion coefficients, since many of OCAs are not fluorescent. These techniques are very appropriate for measuring protein diffusivity in tissues, and since the proteins are widely used for glucose detection the techniques are then important for development of new methods, and for increasing the accuracy of existing ones, of glucose detection and monitoring. The spectroscopic, Raman, and photoacoustic methods have a great potential for measuring OCA diffusion coefficients in tissues because these methods provide excellent sensitivity for OCA detection and monitoring. Methods based on usage of radioactive labels for detecting matter flux are a "gold standard" and, thus, are widely used for

measurements of chemicals and drug delivery [71, 73, 74]. However, radioactive labeling methods cannot always be used for living tissues. The measurement of the temporal changes of scattering properties of a tissue has been proposed recently for OCA diffusion and permeability coefficients estimation [52, 60, 68, 98, 100, 101].

Below, we discuss two methods based on measurement of temporal changes of the scattering properties of a tissue: (i) spectroscopy and (ii) optical coherence tomography.

7.5.1 Spectroscopic Methods

The transport of low-molecular OCAs within tissue can be described in the framework of a free diffusion model [52, 71, 73, 74, 95–98]. It is assumed that the following approximations are valid for the transport process: (i) only concentration diffusion takes place; that is, the flux of the agent into tissue at a certain point within the tissue sample is proportional to the agent concentration at this point; (ii) the diffusion coefficient is constant over the entire sample volume; (iii) penetration of the agent into a tissue sample does not change the agent concentration in the external volume; (iv) during diffusion the agent does not interact with tissue components.

Geometrically, the tissue sample can be presented as an infinite plane-parallel slab with a finite thickness. In this case, the one-dimensional diffusion problem can be considered. The one-dimensional diffusion equation of an OCA transport has a form (Fick's second law):

$$\frac{\partial C(x,t)}{\partial t} = D\frac{\partial^2 C(x,t)}{\partial x^2} \tag{7.8}$$

where

$C(x,t)$ is the agent concentration,
D is the diffusion coefficient,
t is the time,
x is the spatial coordinate.

Depending on the analytical solution used, tissue type, and the experimental setup, different kinds of initial and boundary conditions are used for studies of agent transport in tissues [52, 58, 63, 95, 98, 102].

The initial condition corresponds to the absence of an agent inside the tissue before the measurements, that is:

$$C(x,0) = 0 \tag{7.9}$$

for all inner points of the tissue sample.

When a penetrating agent is administered to tissue topically and the tissue is a semi-infinite medium, that is, $x \in [0;\infty)$, the boundary conditions have the form:

$$C(0,t) = C_0 \quad \text{and} \quad C(\infty,t) = 0 \tag{7.10}$$

Solution of Eq. (7.8) with the initial [Eq. (7.9)] and the boundary [Eq. (7.10)] conditions has the form [103]:

$$C(x,t) = C_0\left[1-\mathrm{erf}\left(\frac{x}{2\sqrt{Dt}}\right)\right] \tag{7.11}$$

where:

$$\mathrm{erf}(z) = \frac{2}{\sqrt{\pi}}\int_0^z \exp(-a^2)\mathrm{d}a$$

is the error function.

Experimentally, the simplest method for estimation of diffusion coefficients of liquids in tissues is based on the time-dependent measurement of collimated transmittance of tissue samples placed in an immersion liquid (Figure 7.4) [52]. Collimated transmittance could be measured in the wide wavelength range using commercially available spectrophotometers with an internal integrating sphere [46, 57–59, 61] or fiber-optic grating-array spectrometers [49, 52, 57, 60, 68, 89].

The time dependent collimated transmittance of a tissue sample impregnated by an OCA can be derived from the Bouguer–Lambert law:

$$T_c(t) = (1-R_s)^2 \exp\{-[\mu_a + \mu_s(t)]l(t)\} \tag{7.12}$$

where

R_s is the specular reflectance,
μ_a is the tissue absorption coefficient,
$\mu_s(t)$ is the tissue time-dependent scattering coefficient,
$l(t)$ is the time-dependent thickness of the tissue sample.

The time dependence of the tissue thickness occurs due to osmotic activity of immersion agents. In general, application of OCAs can be accompanied by tissue shrinkage or swelling, which should be taken into account.

Volumetric changes of a tissue sample are mostly due to changes in sample thickness $l(t)$, which can be expressed as [52]:

$$l(t) = l(t=0) \pm A^*[1-\exp(-t/\tau_s)] \tag{7.13}$$

where $A^* = A/S$, and S is the tissue sample area. The constants A and τ_s can be obtained from direct measurements of thickness or volume of tissue samples and from time-dependent weight measurements. In the equation a "plus" sign corresponds to increasing sample volume, that is, a swelling process, and a "minus" sign corresponds to decreasing sample volume, that is, shrinkage. For example, for dura mater samples immersed in the mannitol solution, parameter A is estimated to be 0.21 and the parameter characterizing the swelling rate, that is, τ_s is 484 s [52].

By the changing volume of a tissue the swelling (shrinkage) produces the change in volume fraction of the tissue scatterers, and thus the change of the scatterer packing factor and the numerical concentration (density or volume fraction), that is, number

of the scattering particles per unit area (for long cylindrical particles, density fraction) or number of the scattering particles per unit volume (for spherical particles, volume fraction). The temporal dependence of the volume fraction of the tissue scatterers is described as [52]:

$$\phi(t) = \frac{V_s}{V(t)} = \frac{\phi(t=0) \times V(t=0)}{V(t=0) \pm A[1-\exp(-t/\tau)]} \tag{7.14}$$

where V_s is the volume fraction of the tissue sample scatterers.

The optical model of many fibrous tissues can be presented as a slab with a thickness l containing scatterers (collagen fibrils) – thin dielectric cylinders with an average diameter of 10–400 nm [3], which is considerably smaller than their lengths, which can be a few millimeters. These cylinders are located in planes, which are parallel to the sample surfaces, but within each plane their orientations are random. In addition to the small so-called Rayleigh scatterers, the fibrils are arranged in individual bundles in a parallel fashion; moreover, within each bundle, the groups of fibers are separated from each other by large empty lacunae distributed randomly in space [3, 4]. In eye sclera collagen bundles show a wide range of widths (1–50 μm) and thicknesses (0.5–6 μm) [104].

For non-interacting particles the time-dependent scattering coefficient, $\mu_s(t)$, of a tissue is defined by the following equation:

$$\mu_s(t) = N(t)\sigma_s(t) \tag{7.15}$$

where $N(t)$ is the number of the scattering particles (fibrils) per unit area and $\sigma_s(t)$ is the time-dependent cross-section of scattering. The number of the scattering particles per unit area can be estimated as $N(t) = \phi(t)/(\pi a^2)$ [105], where a is the radius of the tissue scatterers. For typical intact fibrous tissues, such as sclera, dura mater, and skin dermis, ϕ is usually 0.2–0.3 [3].

To take into account interparticle correlation effects that are important for tissues with densely packed scattering particles the scattering cross-section has to be corrected by the packing factor of the scattering particles, $[1-\phi(t)]^{p+1}/[1+\phi(t)(p-1)]^{p-1}$ [106], where p is the packing dimension that describes the rate at which the empty space between scatterers diminishes as the total number density increases. For spherical particles the packing dimension is equal to 3, and the packing of sheet-like and rod-shaped particles is characterized by packing dimensions that approach 1 and 2, respectively. Thus, Eq. (7.15) has to be rewritten as:

$$\mu_s(t) = \frac{\phi(t)}{\pi a^2}\sigma_s(t)\frac{[1-\phi(t)]^3}{1+\phi(t)} \tag{7.16}$$

The time dependence of the refractive index of the interstitial fluid can be derived using the law of Gladstone and Dale, which states that the resulting value represents an average of the refractive indices of the components related to their volume fractions [66]. Such dependence is defined as:

$$n_I(t) = [1-C(t)]n_{base} + C(t)n_{oca} \tag{7.17}$$

where n_{base} is the refractive index of the tissue interstitial fluid at the initial moment, and n_{oca} is the refractive index of the OCA. The wavelength dependence of water has been presented in Reference [107] in visible and near-infrared (NIR) regions:

$$n_w(\lambda) = 1.3199 + \frac{6.878 \times 10^3}{\lambda^2} - \frac{1.132 \times 10^9}{\lambda^4} + \frac{1.11 \times 10^{14}}{\lambda^6} \tag{7.18}$$

As a first approximation, we can assume that during the interaction between the tissue and the immersion liquid the size and refractive index of the scatterers does not change. Glycosaminoglycans are charged with tissue hydration because of the formation of hydration shells. Therefore, the fibrils preferentially absorb the initial water and then remain at a relatively constant diameter [5, 51].

In this case, all changes in the tissue scattering are connected with the changes of the refractive index of the interstitial fluid described by Eq. (7.17).

The set of equations describing the dependence of OCA concentration on time represents the direct problem. Reconstruction of the diffusion coefficient of OCA can be carried out on the basis of measurement of the temporal evolution of the collimated transmittance. The solution of the inverse problem can be obtained by minimization of the target function:

$$F(D) = \sum_{i=1}^{N_t} \left[T_c(D, t_i) - T_c^*(t_i)\right]^2$$

where $T_c(D, t)$ and $T_c^*(t)$ are the calculated and experimental values of the time-dependent collimated transmittance, respectively, and N_t is the number of measurements corresponding to different time intervals at registration of the temporal kinetics of the collimated transmittance [52, 98, 108].

For *in vivo* studies, one can use the back reflectance geometry to provide measurements (Figure 7.6). For this, fiber-optic grating-array spectrometers are suitable because of their fast spectra collection during immersion agent action [29, 46, 60, 63, 68, 89]. Measured temporal evolution of the tissue optical reflectance could be used to calculate the OCA diffusion coefficient. The inverse problem can be solved by minimization of the target function:

$$F(D) = \sum_{i=1}^{N_t} \left[R(D, t_i) - R^*(t_i)\right]^2$$

where $R(D, t)$ and $R^*(t)$ are the calculated and experimental values of the time-dependent reflectance, respectively, and N_t is the number of measurements corresponding to different time intervals at registration of the temporal kinetics of the reflectance [68].

7.5.2 Optical Coherence Tomography

OCT is an imaging technique that provides images of tissues with a resolution of about 2–10 μm or less at a depth equal to or more than 1 mm depending on the

optical properties of the tissue [56, 100, 101, 109–111]. It allows for determination of refractive index and attenuation coefficient in layered structures in skin and other tissues.

Attenuation of light intensity for ballistic photons, I, in a medium with scattering and absorption is described by the Bouguer–Lambert law: $I = I_0 \exp(-2\mu_t z)$, where I_0 is the incident light intensity, $\mu_t = \mu_a + \mu_s$ is the attenuation coefficient for ballistic photons, and $2z$ is the total tissue probing depth due to double pass of tissue layer by ballistic photons. Since absorption in tissues is substantially less than scattering ($\mu_a << \mu_s$) in the NIR spectral range, the exponential attenuation of ballistic photons in tissue depends mainly on the scattering coefficient: $I = I_0 \exp(-2\mu_s z)$ [46]. Since the scattering coefficient of tissue depends on the bulk index of refraction mismatch, an increase in refractive index of the interstitial fluid and a corresponding decrease in scattering can be detected as a change in the slope of fall-off of the depth-resolved OCT amplitude [46, 110].

The permeability coefficient for solutions in tissue layers (membranes) can be measured using two OCT methods: OCT signal slope (OCTSS) and OCT amplitude (OCTA) registration (Figure 7.8). With the OCTSS method, the average permeability coefficient of a specific region in the tissue can be calculated from the measured changes of OCT signal slope caused by agent diffusion. For this a region in the tissue, where the OCT one-dimensional distribution of intensity in-depth (A-scan) is linear and has minimal alterations, has to be selected, and its thickness (z_{region}) has to be measured. Diffusion of the agents in the chosen region can be monitored as a dynamic process (reversible) of the slope alternation, and, thus, time of diffusion can be recorded (t_{region}). The average permeability coefficient of the selected region ($\bar{P}$) can be calculated by dividing the thickness of the selected region by the time it took for the agent to diffuse through this tissue layer $\bar{P} = \left(z_{\text{region}}/t_{\text{region}}\right)$ [101, 110].

Figure 7.9 shows the OCT signal slope as a function of time recorded from sclera in a fully submersed whole eyeballs experiment during glucose diffusion [110]. Immersion of the eyeball by glucose was performed at the seventh min after the onset of the experiment. The diffusion of glucose into sclera changed the local scattering coefficient. The increase in local in-depth glucose concentration resulted in a decrease in OCT signal slope during glucose diffusion, measured from z_{region} of approximately 100 μm. As the glucose diffuses through, the reverse process starts to take place (decrease of glucose concentration as the saline diffuses in), as seen at the 45th minute of the experiment. Therefore, the calculated glucose permeability coefficient ($\bar{P}$)was approximately $5.5 \times 10^{-6}\,\text{cm}\,\text{s}^{-1}$.

The high resolution of the OCT technique allows estimation of the permeability coefficient not only as a function of time but as a function of depth as well. The OCTA method can be used to calculate the permeability coefficient at specific depths in the tissues as $P(z) = z_i/t_{z_i}$, where z_i is the depth at which measurements were performed (distance from the tissue front surface) and t_{z_i} is the time for agent diffusion to that depth. The value of t_{z_i} has to be calculated from the time point when agent was added to the tissue until the time point where agent-induced change in the OCT amplitude commenced [110]. Figure 7.10a shows a typical OCT signal measured at

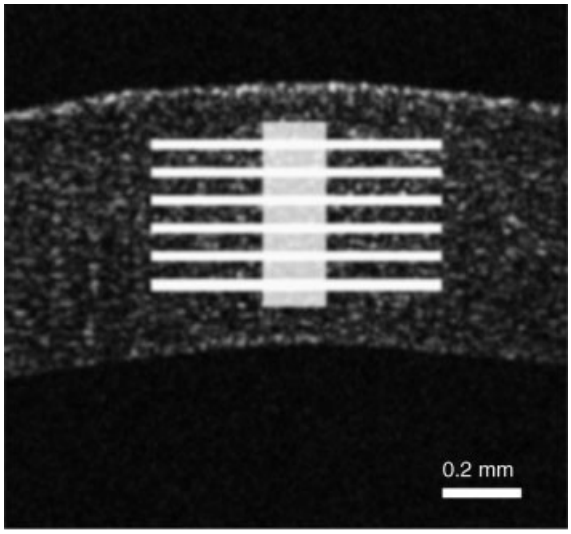

(a)

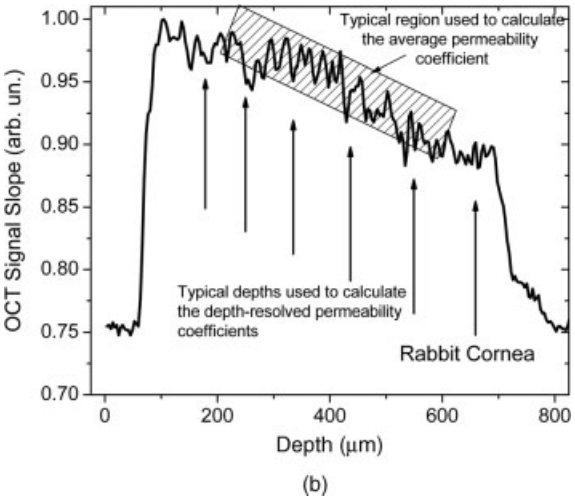

(b)

Figure 7.8 Schematic diagram showing basic principles of two methods used to calculate molecular permeability coefficients. (1) OCT signal slope (OCTSS): calculating the average permeability coefficient in tissues' stroma and computed by dividing the thickness by time – denoted by rectangles in (a) and (b); (2) OCT amplitude (OCTA): calculating the permeability coefficient at different depths, thickness from the epithelial layer to a particular depth, the time is computed from the instant glucose was added until glucose-induced change in the OCT amplitude commenced; denoted by bars in (a) and arrows in (b).

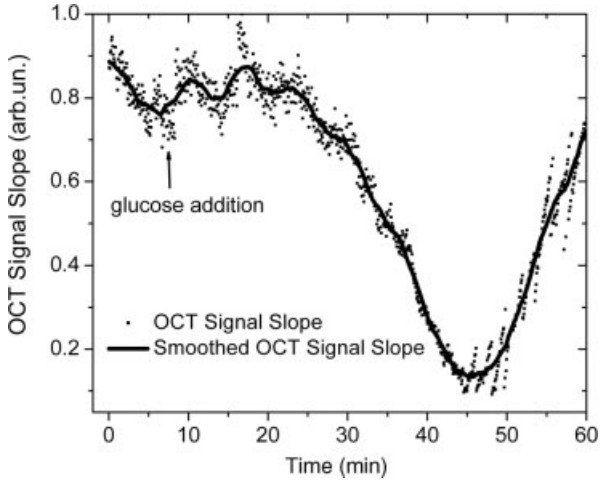

Figure 7.9 OCTSS as a function of time recorded from sclera (fully submersed whole eyeballs experiments) [110] during a glucose diffusion experiment. The arrow indicates when the agent was added.

depths of 105, 158, 225, and 273 μm from the surface of a rabbit sclera during a mannitol diffusion experiment. The arrows on each of the OCT signals depict the time the agent's action reached that particular depth, as illustrated by a sharp decrease of the OCT signal amplitude. Figure 7.10b shows the calculated permeability rates of 20%-mannitol measured at different depths in the sclera. This graph demonstrates that the permeability rate inside the sclera is not homogenous and is increasing with increasing depth, as is expected for multilayered objects with different tissue density. Therefore, the results for depth-resolved quantification of molecular diffusion in tissues demonstrate that the permeability rate inside epithelial tissues is increasing with increasing depth. Several factors are likely to contribute to such an increase in permeability rates with tissue depth: the layered structure of the tissues, the difference in diameters of the collagen fibers in each layer, and the diverse organizational patterns of the collagen bundles at different depths. For instance, the sclera possesses three distinct layers, which include the episclera, stroma, and lamina fusca. The outer layer, the episclera, consists primarily of collagen bundles that intersect at different angles along the surface of the sclera. This inconsistency in organization of the collagen bundles causes a lower permeability rate of the agent, imposing an effective resistance force that potentially reduces the speed of penetration into the tissue. In the stroma and the lamina fusca of the sclera, the collagen fibrils are more organized and oriented in two patterns, meridionally or circularly, reflecting the observed increase in agent permeability in the stroma. The different diameters of the collagen fibers at different tissue depths may also influence the diffusion processes in tissues.

Table 7.2 summarizes both the diffusivity and permeability obtained by the above-described methods.

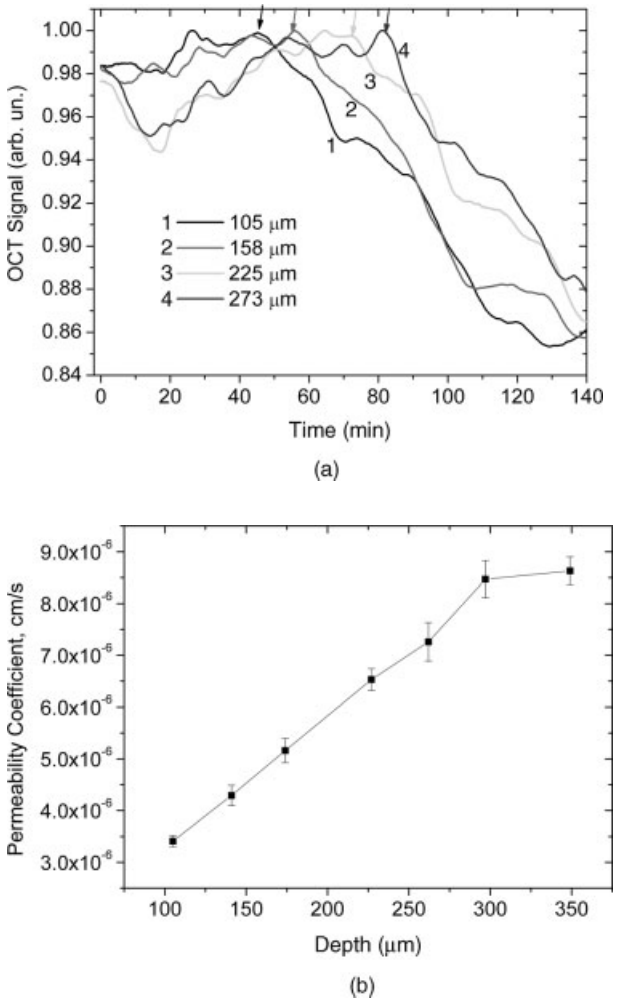

Figure 7.10 (a) OCT signal as a function of time recorded at different depths during a mannitol diffusion experiment in the sclera (arrows indicate the different depths reached by the mannitol front inside a sclera); (b) permeability rates recorded at different depths in a sclera during the diffusion of 20%-mannitol.

OCT has many advantages over other popular imaging systems such as X-ray, MRI, and ultrasound in terms of safety, cost, contrast, and resolution. However, lack of penetration depth into tissue is the main drawback of OCT. The turbidity of most biological tissues could prevent the ability of OCT to be fully engaged in various diagnostic and therapeutic procedures. As described above, application of OCAs can reduce scattering and, thus, improve imaging depth and contrast in OCT imaging of different tissues and cells. As an example, Figure 7.11 shows typical OCT images of

Table 7.2 Diffusivity (D) and permeability (P) of different OCAs in tissues obtained by different methods.

Tissue	OCA	Experimental method[a)]	$D \times 10^{-6}$ ($cm^2 s^{-1}$)	$P \times 10^{-6}$ ($cm^2 s^{-1}$)	Reference
Human sclera *in vitro*	20%-Aqueous glucose solution	CTS	0.57 ± 0.09		[98]
Human sclera *in vitro*	30%-Aqueous glucose solution	CTS	1.47 ± 0.36		[98]
Human sclera *in vitro*	40%-Aqueous glucose solution	CTS	1.52 ± 0.05		[98]
Human dura mater *in vitro*	20%-Aqueous glucose solution	CTS	1.63 ± 0.29		[52]
Human dura mater *in vitro*	20%-Aqueous mannitol solution	CTS	1.31 ± 0.41		[52]
Rat skin *in vitro*	40%-Aqueous glucose solution	CTS	1.1 ± 0.16		[108]
Rabbit sclera *in vivo*	40%-Aqueous glucose solution	ReS	0.54 ± 0.01		[68]
Human skin *in vivo*	40%-Aqueous glucose solution	ReS	2.56 ± 0.13		[60]
Rabbit cornea *in vitro*	Mannitol solution	OCT		8.99 ± 1.43	[100]
Rabbit sclera *in vitro*	Mannitol solution	OCT		6.18 ± 1.08	[100]
Rabbit sclera *in vitro*	20%-Aqueous glucose solution	OCT		8.64 ± 1.12	[100]
Pig aorta *in vitro*	20%-Aqueous glucose solution	OCT		14.3 ± 2.4	[110]
Pig skin *in vitro*	20%-Aqueous glucose solution	OCT		7.69 ± 0.56	[110]
Rhesus monkey skin *in vivo*	20%-Aqueous glucose solution	OCT		2.32 ± 0.2	[101]

a) Abbreviations: CTS, collimated transmittance spectroscopy; ReS, reflectance spectroscopy; OCT, optical coherence tomography.

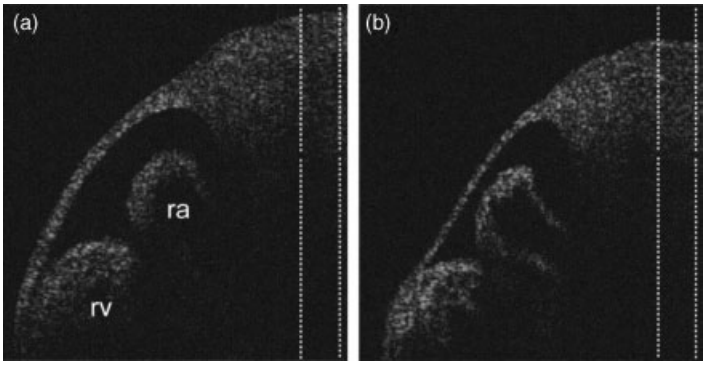

Figure 7.11 Typical OCT images of a mouse embryo acquired before (a) and 10 min after addition of 50% glycerol (b). In (a), ra = right atrium; rv = right ventricle.

the same area of a mouse embryo imaged before and 10 min after the addition of 50% glycerol (Figure 7.11a and b, respectively).

The selected imaging areas contained heart chambers as well as more optically uniform tissues used to assess the clearing effect of introduced clearing agent. As one can see from the images, during glycerol diffusion into the tissue, the atrial wall became more visually defined and the structure of the trabeculae within the ventricle became more distinguishable. Scans through the more uniform abdominal region (marked with vertical lines in Figure 7.11) were used to assess the degree of optical clearing. The percentage of signal enhancement at depths of 200 to 500 μm from the surface was calculated to be $51.5 \pm 12.5\%$ at about 10–15 min after addition of glycerol. Interestingly, the OCT signal amplitude in the upper tissue layers (up to 100 μm from the surface) is lower than that before the application of the glycerol (Figure 7.12). In the deeper layers the addition of glycerol caused an increase of the OCT signal amplitude. This result is consistent with the expectations from layer-by-layer optical clearing: the diffusion of the OCA into the tissue decreases back scattering at the upper layers by eliminating the refractive index mismatch at tissue and fluid interfaces. Consequently, because scattering is decreased in upper layers, more photons can reach deeper tissue layers, resulting in a higher OCT signal.

7.6 Applications of Tissue Optical Clearing to Different Diagnostic and Therapeutic Techniques

Over the last decade, noninvasive or minimally invasive spectroscopy and imaging techniques have found wide spread application in biomedical diagnostics, for example, OCT [3, 109–111], visible light and NIR spectroscopy [3, 112, 113], fluorescent [28–30] and polarization spectroscopy [3, 69, 114], and others. Spectroscopic

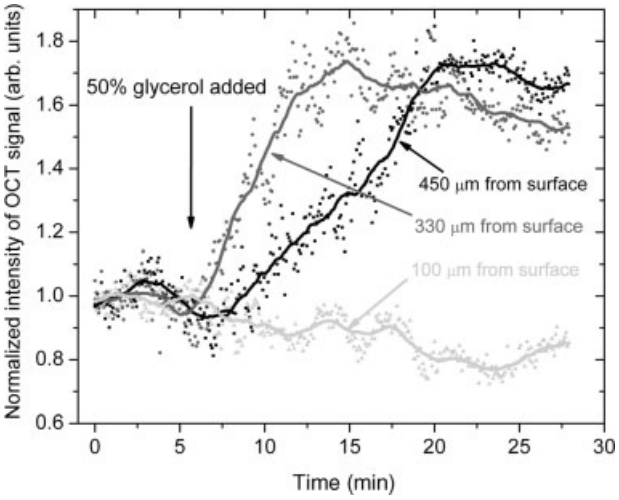

Figure 7.12 Normalized intensity of OCT signal at different depths from the surface as a function of time during addition of glycerol.

techniques can provide a deep imaging of tissues that could give information on blood oxygenation [118] and detect cutaneous and breast tumors [114, 115], whereas confocal microscopy [1, 116–118], OCT [3, 109–111], and multiphoton excitation imaging [1, 117, 119] have been used to show cellular and subcellular details of superficial living tissues. Spectroscopic, OCT, and photoacoustic techniques are applicable for blood glucose monitoring with diabetic patients [3, 120–132].

The reduction of light scattering by a tissue gives not only improvement of image quality and precision of spectroscopic information but decreases irradiating light beam distortion and gives sharp focusing.

We now discuss the application of the immersion technique to several diagnostic and therapeutic applications.

7.6.1 Glucose Sensing

7.6.1.1 NIR Technique

Measurements of blood glucose and its regulation are necessary for patients with disorders of their carbohydrate metabolism, particularly caused by diabetes mellitus [121]. In recent decades, noninvasive blood glucose monitoring has become an increasingly important topic in the realm of biomedical engineering. In particular, the introduction of optical approaches has brought exciting advances to this field [122].

NIR spectroscopy has potential in realizing noninvasive blood glucose monitoring. The NIR region is ideal for the noninvasive measurement of human body compositions because biological tissue is relatively transparent to light in this region, the

so-called therapeutic window. The molecular formula of glucose is $C_6H_{12}O_6$ and several hydroxyl and methyl groups are contained in this structure. They are mainly hydrogen functional groups whose absorption occurs in the NIR region. For glucose, the second overtone absorption is in the spectral region between 1100 and 1300 nm and the first overtone absorption is in the region 1500–1800 nm [122]. In the range 1400–1500 nm there is a peak that corresponds to the absorption peak of water [133]. This information provides the theoretical basis for the measurement of blood glucose using NIR spectroscopy [122, 123]. Moreover, tissue optical clearing can be helpful for more contrast visualization of glucose bands in tissue reflectance spectra. For example, selection of an OCA without the peak in the range around 1600 nm can provide dehydration of tissue and, thereby, decrease the water peak. In contrast, glucose peak at 1600 nm can be better differentiated.

Noninvasive NIR blood glucose monitoring is a challenge because it deals with very weak signals of glucose directly from human skin, and the physiological conditions of skin that may influence on detected signal, such as body temperature, vary easily with time. However, glucose injection produces body temperature changes [134]. There is a potential for a coincidental correlation between the circadian fluctuation of glucose concentration in human blood and the circadian periodicity of the body temperature and other vital signs. Correlation between glucose concentrations and temperature-modulated localized reflectance signals at wavelengths between 590 and 935 nm, where there are no known NIR glucose absorption bands, has been presented in Reference [120].

One critical difficulty associated with *in vivo* blood glucose assay is an extremely low signal-to noise ratio of glucose peak in an NIR spectrum of human skin tissue. Therefore, the main problem of the NIR glucose monitoring is the construction of calibration models [112, 113, 122, 123].

The calibration models developed from oral glucose intake types of experiments often have chance temporal correlation. At present, the utilization of plural experiment data sets for quantitative modeling is most useful to avoid the chance temporal correlation. In Reference [112] partial least-squares regression was carried out for the NIR data (total 250 paired data-set) and calibration models were built for each subject individually. The selection of informative regions in NIR spectra for analysis can significantly refine the performance of these full-spectrum calibration techniques [113].

The floating-reference method of calibration is described in Reference [122]. The key factor and precondition of the method are the existence of the reference position where diffuse reflectance light is not sensitive to the variations of glucose concentration. Using the signal at the reference position as the internal reference for human body measurement can improve the specification for extraction of glucose information [122].

The concept of noninvasive blood glucose sensing using the scattering properties of blood is an alternative to the spectral absorption method [124]. The method of NIR frequency-domain reflectance techniques is based on changes in glucose concentration, which affects the refractive index mismatch between the interstitial fluid and tissue fibers, and hence μ_s' [125]. A glucose clamp experiment (the concentrations of

injected glucose and insulin are manipulated to result in a steady concentration of glucose ever a period of time [120]) showed that $\delta\mu_s'$ at 650 nm (the distances between the source- and detector-fibers $r_{sd} = 1$–10 mm) qualitatively tracked changes in blood glucose concentration for a volunteer with diabetes [126].

The response of a non-diabetic male subject to a glucose load of 1.75 g per kg body weight, as a standard glucose tolerance test, was determined by continuously monitoring the product of $n\mu_s'$ measured on muscle tissue of the subject's thigh using a portable frequency-domain spectrometer [125]. The refractive index n of the interstitial fluid modified by glucose is defined by the equation [125] $n_{glw} = n_w + 1.515 \times 10^{-6} \times C_{gl}$, where C_{gl} is glucose concentration in mg dl^{-1} and n_w is the refractive index of water [107]. As the subject's blood glucose rose, the $n\mu_s'$ decreased. Key factors for the success of this approach are the precision of the measurements of the reduced scattering coefficient and the separation of the scattering changes from absorption changes, as obtained with the NIR frequency-domain spectrometer [125]. Evidently, other physiological effects related to glucose concentration could account for the observed variations of μ_s' and, as mentioned earlier, the effect of glucose on the blood flow in the tissue may be one of the sources of the errors of μ_s' measurements.

7.6.1.2 **OCT Technique**

The OCT method described in Section 7.5.2 can also be used for glucose monitoring in tissues. Since the OCT technique measures the in-depth distribution of reflected light with a high spatial resolution, changes in the in-depth distribution of the tissue scattering coefficient and/or refractive index mismatch affect the OCT signal parameters – slope and amplitude. Free blood glucose perfusion via blood capillaries and subsequent diffusion in tissues induce local changes of optical properties (scattering coefficient and refractive index); thus one can monitor and quantify the diffusion process by depth-resolved analyses of the OCT signal recorded from a tissue site [101, 110, 111, 127, 128]. Physiological glucose levels are in the range 3–30 mM, which is far below the level of making the tissue transparent. However, OCT can detect photons backscattered from different layers in the sample. Thus, changes in the scattering properties can be studied at different depths in the sample [56]. Therefore, a high sensitivity of the OCT signal from living tissues to glucose content allows one to monitor its concentration in the skin at a physiological level [127, 128].

7.6.1.3 **Photoacoustic Technique**

Both *in vitro* and *in vivo* studies have been carried out in the spectral range of the transparent "tissue window," around the 1–2 μm, to assess the feasibility of photoacoustic spectroscopy (PAS) for noninvasive glucose detection [129]. The photoacoustic signal is obtained by probing the sample with monochromatic radiation, which is modulated or pulsed. Absorption of probe radiation by the sample results in localized short-duration heating. Thermal expansion then gives rise to a pressure wave, which can be detected with a suitable transducer. An absorption spectrum for the sample can be obtained by recording the amplitude of generated pressure waves

as a function of probe beam wavelength [129]. The pulsed PA signal is related to the properties of a turbid medium by the equation [120, 129]:

$$\mathrm{PA} = k(\beta \upsilon^n / C_p) E_0 \mu_{\mathrm{eff}}$$

where

PA is the signal amplitude,
k is the proportionality constant,
E_0 is the incident pulse energy,
β is the coefficient of volumetric thermal expansion,
υ is the speed of sound in the medium,
C_p is the specific heat capacity,
n is a constant between one and two, depending on the particular experimental conditions,
$\mu_{\mathrm{eff}} = \sqrt{3\mu_a(\mu_a + \mu_s')}$.

In the PAS technique, the effect of glucose can be analyzed by detecting changes in the peak-to-peak value of laser-induced pressure waves [130].

The investigations have demonstrated the applicability of PAS to the measurement of glucose concentration [130, 131]. The greatest percentage change in the photoacoustic response was observed in region of the C−H second overtone at 1126 nm, with a further peak in the region of the second O−H overtone at 939 nm [129]. In addition, the generated pulsed PA time profile can be analyzed to detect the effect of glucose on tissue scattering, which is reduced by increasing glucose concentration [46, 120].

A new concept for *in vivo* glucose detection in the mid-infrared spectral range is based on the use of two-quantum cascade lasers emitting at wavelengths 9.26 and 9.38 μm to produce PA signals in the forearm skin [132]. One of the wavelengths correlates with glucose absorption, while the other does not. Determination of glucose concentration in the extracellular fluid of the stratum spinosum permits deduction of the glucose concentration in blood, because the two factors correlate closely with each other. This method allows us to improve glucose specificity and to remove the effect of other blood substances.

7.6.1.4 **Raman Spectroscopy**

Raman spectroscopy (RS) can provide potentially rapid, precise, and accurate analysis of OCA concentration and biochemical composition. RS provides information about the inelastic scattering, which occurs when vibrational or rotational energy of target molecules is exchanged with incident probe radiation. Raman spectra can be utilized to identify molecules such as glucose, because these spectra are characteristic of variations in the molecular polarizability and dipole momentum. Enejder *et al.* [135] have accurately measured glucose concentrations in 17 non-diabetic volunteers following an oral glucose tolerance protocol.

In contrast to infrared and NIR spectroscopies, Raman spectroscopy has a spectral signature that is less affected by water, which is very important for tissue study. In

addition, Raman spectral bands are considerably narrower (typically 10–20 cm^{-1} wide [136]) than those produced in NIR spectral experiments. The RS also has the ability for simultaneous estimation of multiple analytes, requires minimum sample preparation, and would allow for direct sample analysis [137]. Like infrared absorption spectra, Raman spectra exhibit highly specific bands, which are dependent on concentration. As a rule, for Raman analysis of tissue, the spectral region between 400 and 2000 cm^{-1}, commonly referred to as the "fingerprint region," is employed. Different molecular vibrations lead to Raman scattering in this part of the spectrum. In many cases bands can be assigned to specific molecular vibrations or molecular species, aiding the interpretation of the spectra in terms of biochemical composition of the tissue [137].

Because of the reduction of elastic light scattering at tissue optical clearing, more effective interaction of a probing laser beam with the target molecules is expected. The OCAs increase the signal-to-noise ratio, reduce the systematic error incurred as a result of incompletely resolved surface and subsurface spectra, and significantly improve the Raman signal [96].

7.6.2 Tissue Imaging

7.6.2.1 Confocal Microscopy

Reflection confocal microscopy (RCM) is widely used at present in various biomedical investigations for visualization of the internal structure of biological tissues on a cellular and subcellular level [116, 117]. A confocal microscope illuminates and detects the scattered or fluorescent light from the same volume within the specimen. The main advantage of RCM is its ability to optically section thick specimens [117]. This technique makes it possible to obtain high-quality (with a micrometer spatial resolution) images of cellular layers. A high image contrast and a high spatial resolution of RCM are achieved due to probing a small volume of the medium bounded by the size of the central focal spot, which is formed by a focusing optical system. The main limitation of the confocal microscopy in skin studies is high scattering that distorts the quality of cell images. The increase in transparency of the upper skin layers can improve the penetration depth, image contrast, and spatial resolution of confocal microscopy [118].

Using Monte Carlo simulation of the point spread function it was shown that confocal microscopic probing of skin at optical clearing is potentially useful for deep reticular dermis monitoring and improving the image contrast and spatial resolution of the upper cell layers [118].

7.6.2.2 Nonlinear Microscopy

Optical clearing seems to be a promising technique for improvement of detected signals in nonlinear spectroscopy. In Reference [138] the authors have examined the effect of optical clearing with glycerol to achieve greater in-depth imaging of specimens of skeletal muscle tissue and mouse tendon (collagen based) by three-dimensional (3D) second-harmonic generation (SHG) imaging microscopy. It was

found that treatment with 50%-glycerol results in a 2.5-fold increase in the SHG imaging depth. In Reference [139] it was also shown that the axial attenuation of the forward SHG signal decreases with increasing glycerol concentration (25%, 50%, and 75%). This response results from the combination of the primary and secondary filter effects on the SHG creation and propagation, respectively [139]. The authors of Reference [139] note that the application of glycerol results in a swelling of the muscle cells, where the higher concentrations result in thicker tissues for the same exposure time. The tendon also exhibits significant swelling on immersion in glycerol solutions.

Thus, it was shown that reduction of the primary filter following glycerol treatment dominates the axial attenuation response in both muscle and tendon. However, these disparate tissue types have been shown to clear through different mechanisms of the glycerol–tissue interaction. In the a-cellular tendon, glycerol application reduces scattering by both index matching as well an increasing the inter-fibril separation. Through analysis of the axial response as a function of glycerol concentration in striated muscle, the authors conclude that the mechanism in this tissue arises from matching of the refractive index of the cytoplasm of the muscle cells with that of the surrounding higher index collagenous perimysium [139].

Collagen fibers produce a high second-harmonic signal and can be imaged inside skin dermis with SHG microscopy [140]. Evidently, due to optical clearing, less scattering in the epidermis for the incident long wavelength light (800 nm) and especially for the backward SHG short wavelength light (400 nm) may improve SHG images of dermis collagen structures [46].

However, at 100%-glycerol application to rodent skin dermis and tendon samples, as well as to engineered tissue model (raft), a high efficiency of tissue optical clearing was achieved in the wavelength range 400–700 nm, but the SHG signal was significantly degraded in the course of glycerol application and returned back to the initial state after tissue rehydration by application of saline [64]. The loss of SHG signal in Reference [64] is associated with the reversible dissociation of collagen fibers and the corresponding loss of fibril organization on glycerol action. Such an explanation is somewhat contradictory, because less organization of collagen fibers will lead to higher scattering [46]. Since the significant effect of optical clearing at glycerol application is tissue dehydration, an explanation following from data of Reference [140] seems to be more adequate. Using reflection-type SHG polarimetry, it was shown in Reference [140] that the SHG polarization signal for chicken skin dermis was almost unchanged and the SHG intensity was decreased to about a quarter at tissue dehydration. The authors have hypothesized that the decrease of SHG intensity results in a change of linear optical properties, that is, scattering efficiency (reduction of the SHG photon recycling), rather than of efficiency of SHG in the tissues.

It is possible that SHG and optical clearing may provide an ideal mechanism to study physiology in highly scattering skeletal or cardiac muscle tissue with significantly improved depth of penetration and achievable imaging depth. However, the problem of the change of SHG signal on the optical clearing of fibrous tissue as skin, sclera, and others requires further research.

7.6.2.3 Multiphoton Microscopy

The application of OCAs may prove to be particularly relevant for enhancing two-photon microscopy [141], since it has been shown that the effect of scattering is to drastically reduce penetration depth to less than that of the equivalent single-photon fluorescence while largely leaving resolution unchanged [117, 119]. This happens mostly due to excitation beam defocusing (distortion) in the scattering media. On the other hand, this technique is useful in understanding the molecular mechanism of tissue optical clearing upon immersion and dehydration.

The first demonstration of two-photon in-depth signal improvement using optical immersion technique with hyperosmotic agents, such as glycerol, propylene glycol, both in anhydrous form, and aqueous glucose solution, was performed by authors of Reference [141] in *ex vivo* experiments with human dermis. Such improvements were obtained within a few minutes of application. The images in Figure 7.13 show the evolution in time of a section at 60 μm depth, after immersion in glycerol [141].

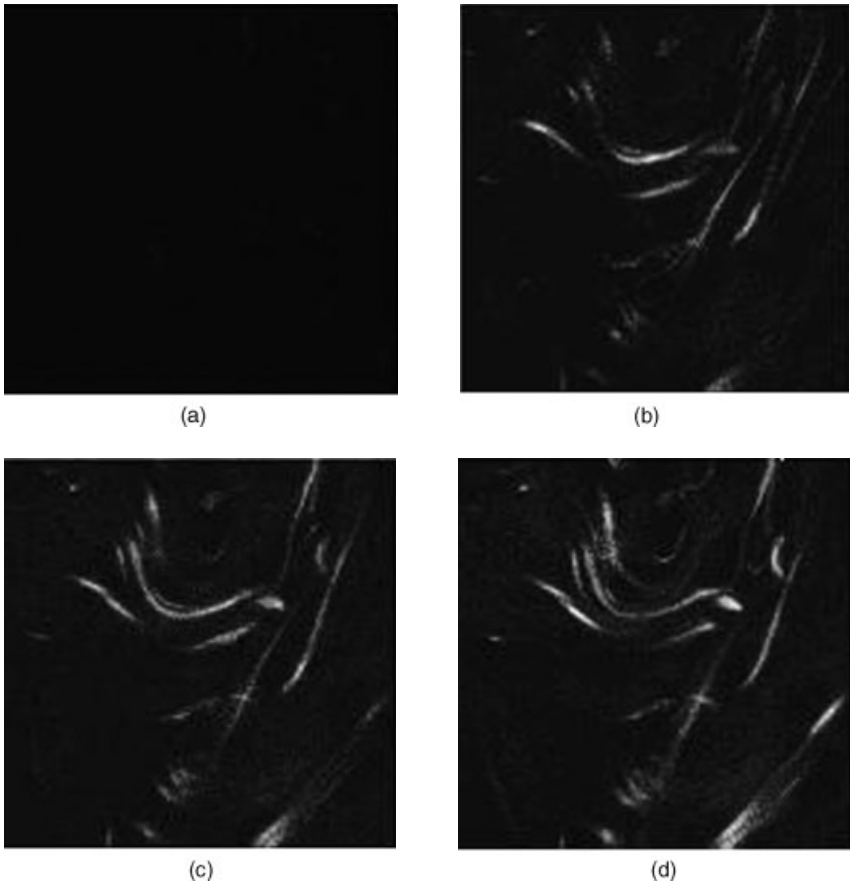

Figure 7.13 Time-lapse sequence of images at 60 μm depth in a skin sample, for immersion in glycerol at time $t = 0$ (a), 120 (b), 240 (c), and 420 s (d) [141].

Before data acquisition, the sample was immersed in 0.1 ml of phosphate-buffered saline (PBS) to prevent drying and shrinkage. Then, the sample was immersed in 0.5 ml of an OCA and one image stack was acquired every 30 s for 6–7 min. Finally, the OCA was removed and the sample was immersed again in 0.1 ml of PBS, to observe the reversibility of the clearing process. The upper limit of tissue shrinkage was estimated as 2% in the course of 6–7 min of OCA application. Only for glycerol was the effect shown to be partially reversible through reapplication of PBS. This adds some support to the hypothesis of alteration to the collagen structure as being a significant contributor to the clearing effect.

The average contrast in each image and relative contrast (RC) were defined as [141]:

$$\text{Contrast} = \sum_{i,j=1}^{N_{\text{lines}}} \left| I_{i,j} - \left\langle I_{i,j} \right\rangle \right|, \quad \text{RC} = 100 \frac{\text{Contrast[OCA]} - \text{Contrast[PBS]}}{\text{Contrast[PBS]}} \tag{7.19}$$

where $\left\langle I_{i,j} \right\rangle$ is the mean intensity of the nearest eight pixels and $N_{\text{lines}} = N - 2$, with $N = 500$; Contrast[OCA] and Contrast[PBS] are calculated using Eq. (7.19), for OCA and PBS immersion, respectively. The values of RC served for comparison purposes.

Of the three agents, glycerol was the most efficient with respect to saturation level (RC = 16.3 at 20 μm depth), but also the slowest. Propylene glycol was similarly efficient (RC = 12.6 at 20 μm depth), whereas, glucose was the worst (RC = 5.1 at 20 μm depth) but diffuses three times faster than glycerol and five times faster than propylene glycol. The RC dramatically increased with increasing depth.

The effect on deeper layers is greater because of the cumulative effect of the reduction in scattering in the superficial layers of the tissue sample, which provides less attenuation of the incident and detected fluorescent light. The contrast is also dependent on fluorescence intensity, which is proportional to the squared intensity of the excitation intensity and mostly dependent on excitation beam focusing ability. Better focusing (less focused beam distortion) is achieved in less scattering media [141].

Additional morphological information is provided by combination of SHG microscopy with two-photon excitation fluorescence microscopy [142]. Nonlinear laser imaging can be improved at tissue optical clearing but requires further investigations.

7.6.2.4 **Polarized Microscopy**

Practically all healthy connective and vascular tissues show the strong or weak optical anisotropy typical for either uniaxial or biaxial crystals [143]. Pathological tissues as a rule show isotropic optical properties because of irregularities of tissue structure (more chaotic cell structures and blood vessel supply network) [144]. Reduction of scattering upon optical immersion makes it possible to detect the polarization anisotropy of tissues more easily and to separate the effects of light scattering and intrinsic birefringence on the tissue polarization properties. It is also possible to study birefringence of form with optical immersion, but when the immersion is strong the average refractive index of the tissue structure is close to the index of the ground media, and the birefringence of form may be too small to be detected [26].

The OCA-induced optical clearing leads to increasing depolarization length. Clearing has a similar impact on scattering and correspondingly on the improvement of polarization properties with increasing efficiency from longer to shorter wavelengths [69]. Owing to less scattering of the longer wavelengths, the initial polarization degree is higher for these wavelengths and thus clearing efficiency is not large; however, the absolute values of achieved polarization degree of transmitted light are the highest.

With the reduction of scattering, tissue birefringence can be measured more precisely. In particular, the birefringence of form and material can be separated. For example, in a translucent human scleral sample impregnated with a highly concentrated glucose solution (about 70%), the measured optical anisotropy $\Delta n = (n_e - n_o)$ was $\sim 10^{-3}$ [26].

7.6.2.5 Optical Projection Tomography

Optical projection tomography (OPT) is a new approach for 3D imaging of small biological specimens. It fills an imaging gap between magnetic resonance imaging and confocal microscopy, being most suited to specimens that are 1–10 mm across [145].

The ability to analyze the organization of biological tissue in three dimensions has proven to be invaluable in understanding embryo development, a complex process in which tissues undergo an intricate sequence of movements relative to each other. A related goal is the mapping of gene expression patterns onto these 3D tissue descriptions. This information provides clues about the biological functions of genes and also indicates which genes may interact with each other [146]. Because OPT can record both absorption and emission profiles, it is able to image the wealth of different staining techniques that exist to record the spatial distribution of gene activity. The most common assay for gene activity at the RNA level is still a protocol that produces a purple precipitate within the tissue. Because this precipitate is not fluorescent, it cannot be imaged by confocal microscopy. However, in bright-field mode, OPT can recreate the 3D distribution of this precipitate for a complete 11.5 dpc (days-post-coitum) mouse embryo [145, 146]. Other important applications for OPT are to help analyze normal and abnormal morphology and to localize where labeled cells are within a tissue [145].

The most common approach for OPT imaging is to suspend the specimen in an index-matching liquid to reduce the scattering of light on the surface and reduce heterogeneities of refractive index throughout the specimen. This means that light passes through the specimen in approximately straight lines and a standard back-projection algorithm can generate relatively high-resolution images [145].

7.6.3 Therapeutic Applications

In vivo control of tissue optical properties can be very important for some therapeutic applications.

In Reference [68] scattering and absorption of different layers of eye under the action of 40%-glucose solution have been simulated by Monte Carlo method. The

modeling has shown that the mean increase of the fraction of photons absorbed in retina at the clearing of sclera is about 30%. Thus, scleral optical clearing may provide more precise and effective coagulation of retinal pigmented epithelium and choroid layers.

Experiments have shown that OCAs (in particular, glycerol) can be used to significantly reduce the radiant exposures required for cutaneous and epidermal blood vessel coagulation [147, 148] and tattoo removal [92, 93, 149, 150].

In many cases, targeted deep blood vessels in a lesion are not sufficiently heated by incident light due to competition from absorption and scattering by other tissue constituents. The skin optical clearing method was proposed makes it possible to observe dermal blood vessel through the intact skin [147, 148]. Subcutaneous radiant exposures for vessels treated with glycerol were typically several-fold lower than untreated vessels. For example, arterioles in the 80–110-μm-diameter range in untreated skin had radiant exposure values of $\sim$12 J cm^{-2}, compared to $\sim$2 J cm^{-2} in glycerol-treated cases [147].

To estimate the effectiveness of laser radiation delivery to the area of the target absorber localization, computer simulation of the alteration of skin optical properties was carried out by Monte Carlo modeling (Figure 7.14). The optical clearing of different skin layers was simulated using Mie scattering theory [8]. For the skin image analysis, optical parameters at $\lambda = 633$ nm (He-Ne laser irradiation) were used [92]. For the target area representation, an absorbing layer in the form of cross was added to the skin model. The depth of the cross location in the model was chosen as 1 mm and its thickness was 50 μm.

The cross borders in Figure 7.14a look rather fuzzy due to high light scattering by the upper tissue layers. The optical clearing of the layers causes a significant increase in contrast of the images that improves visualization of the target area. To estimate the contrast of obtained images the following formula was used: $K = (R_1 - R_2) \times (R_1 + R_2)^{-1}$, where R_1, R_2 are the skin reflectance outside the cross area and inside it, respectively [92].

Analysis of the absorption object image shows that the largest contrast is achieved at the clearing of the upper layer ($K = 0.4$) (Figure 7.14c), which improves contrast of the image on the background of intact skin 2.6-fold ($K = 0.15$) (Figure 7.14a). Insignificant contrast increase is observed at the total immersion of skin – upper and lower layers ($K = 0.28$) (see Figure 14b), because of relatively less interaction ability of light with absorbers at less multiplicity of scattering [92].

The density of irradiation energy of a frequency-doubled Nd:YAG laser ($\lambda = 532$ nm) used for tattoo removal is 2–4 [151], 3 [150], and 2.6 J cm^{-2} [152]. For a ruby laser ($\lambda = 694$ nm) the energy density is 3.5 [153] or 4–7 J cm^{-2} [151]. The energy density of a Q-switched alexandrite laser ($\lambda = 755$ nm) is 5 [150] and 10–16 J cm^{-2} [152]. For a Q-switched Nd:YAG laser ($\lambda = 1064$ nm) the energy density is 4–8 [151] and 5 J cm^{-2} [152]. In Reference [93] it was shown that to achieve a similar result as those without skin optical clearing, when using OCA the density of laser energy can be reduced by 50–60% depending on the target area localization depth in blue-green spectral range, by 30–40% in the red spectral range, and 10–20% in the NIR spectral range. This allows a decrease in thermal damage of skin.

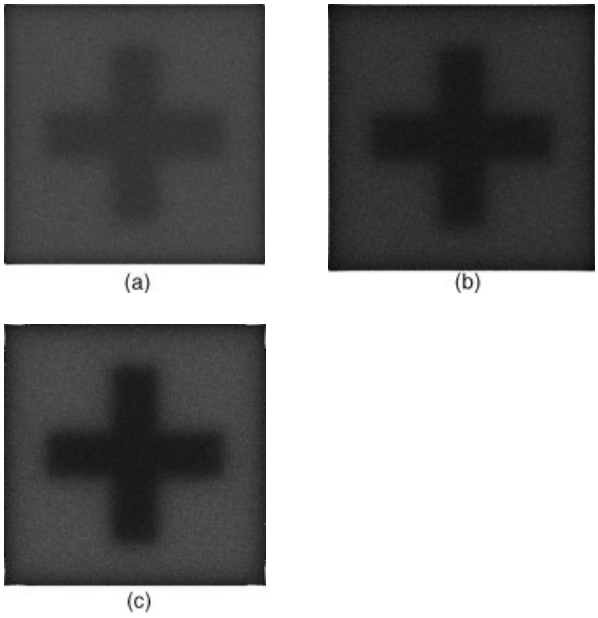

Figure 7.14 Result of Monte Carlo simulation of an image of an absorption layer in skin (cross) at wavelength 633 nm; the layer is 1.0 mm deep, localization of the cross is 1.0mm in depth. Skin without clearing (a); all skin layers (excluding subcutaneous adipose layer) are immersed (b); skin layers above the cross are immersed in glycerol administered topically (c) [92].

7.7 Conclusion

This chapter has demonstrated some specific features of tissue optics and light–tissue interaction. It shows that administration of optical clearing agents allows one to control effectively optical properties of tissues. The control leads to the essential reduction of scattering and therefore causes much higher transmittance (optical clearing) and the appearance of a large amount of least-scattered and ballistic photons, allowing for successful application of different optical imaging and spectroscopic (optical biopsy) techniques for medical purposes. The kinetics of tissue optical clearing, defined, in general, by both the dehydration and agent diffusion processes, is characterized by different time responses that depend on the tissue and agents used. Swelling or shrinkage of the tissue and cells under the action of clearing agents may play an important role in the tissue clearing process.

The immersion technique has great potential for noninvasive medical diagnostics using reflectance spectroscopy, OCT, confocal, nonlinear, polarized microscopy and other methods where scattering is a serious limitation. Optical clearing can increase

the effectiveness of several therapeutic and surgical methods using laser beam action on a target area hindered by depth of a tissue.

Acknowledgment

This work has been supported in part by grant 224014, PHOTONICS4LIFE of FP7-ICT-2007–2; grant 208.2008.2 of President of RF "Supporting of Leading Scientific Schools;" RF Fed. Agen. Education 2.1.1/4989, 2.2.1.1/2950, and 1.4.09; CRDF, RUB1-2932-SR-08, and RFBR N08-02-92224-NNSF (RF-P.R. China).

References

1 Tuchin, V.V. (ed.) (2002) *Handbook of Optical Biomedical Diagnostics*, SPIE Press, Bellingham, PM107.
2 Vo-Dinh, T. (ed.) (2003) *Biomedical Photonics Handbook*, CRC Press, Boca Raton.
3 Tuchin, V.V. (2007) *Tissue Optics: Light Scattering Methods and Instruments for Medical Diagnosis, SPIE Tutorial Texts in Optical Engineering*, Vol. TT38, SPIE Press, Bellingham, Washington.
4 Saidi, I.S., Jacques, S.L., and Tittel, F.K. (1995) Mie and Rayleigh modeling of visible-light scattering in neonatal skin. *Appl. Opt.*, **34** (31), 7410–7418.
5 Culav, E.M., Clark, C.H., and Merrilees, M.J. (1999) Connective tissue: matrix composition and its relevance to physical therapy. *Phys. Therapy*, **79**, 308–319.
6 Schaefer, H. and Redelmeier, T.E. (1996) *Skin Barrier: Principles of Percutaneous Absorption*, Karger, Basel.
7 Young, A.R. (1997) Chromophores in human skin. *Phys. Med. Biol.*, **42**, 789–802.
8 Bohren, C.F. and Huffman, D.R. (1983) *Absorption and Scattering of Light by Small Particles*, John Wiley & Sons, Ltd., New York.
9 Bashkatov, A.N., Genina, E.A., Kochubey, V.I., and Tuchin, V.V. (2005) Optical properties of human skin, subcutaneous and mucous tissues in the wavelength range from 400 to 2000 nm. *J. Phys. D Appl. Phys.*, **38**, 2543–2555.
10 Prahl, S.A. (1988) Light transport in tissue. Ph.D. Thesis, University of Texas at Austin.
11 Chan, E.K., Sorg, B., Protsenko, D., O'Neil, M., Motamedi, M., and Welch, A.J. (1996) Effects of compression on soft tissue optical properties. *IEEE J. Quantum Electron.*, **2**, 943–950.
12 Simpson, C.R., Kohl, M., Essenpreis, M., and Cope, M. (1998) Near-infrared optical properties of *ex vivo* human skin and subcutaneous tissues measured using the Monte Carlo inversion technique. *Phys. Med. Biol.*, **43**, 2465–2478.
13 Du, Y., Hu, X.H., Cariveau, M., Kalmus, G.W., and Lu, J.Q. (2001) Optical properties of porcine skin dermis between 900 nm and 1500 nm. *Phys. Med. Biol.*, **46**, 167–181.
14 Troy, T.L. and Thennadil, S.N. (2001) Optical properties of human skin in the near infrared wavelength range of 1000 to 2200 nm. *J. Biomed. Opt.*, **6**, 167–176.
15 Prahl, S.A. (2009) http://omlc.ogi.edu/spectra/ accessed 1 August 2009).
16 Smith, R.C. and Baker, K.S. (1981) Optical properties of the clearest natural water (200–800 nm). *Appl. Opt.*, **20** (2), 177–184.
17 Bashkatov, A.N., Genina, E.A., Kochubey, V.I., Gavrilova, A.A., Kapralov, S.V., Grishaev, V.A., and Tuchin, V.V. (2007) Optical properties of human stomach mucosa in the spectral range from 400 to 2000 nm: prognosis for gastroenterology. *Med. Laser Appl.*, **22**, 95–104.

18 Bashkatov, A.N., Genina, E.A., Kochubey, V.I., and Tuchin, V.V. (2006) Optical properties of human cranial bone in the spectral range from 800 to 2000 nm. *Proc. SPIE*, **6163**, 616310.

19 Ugryumova, N., Matcher, S.J., and Attenburrow, D.P. (2004) Measurement of bone mineral density via light scattering. *Phys. Med. Biol.*, **49**, 469–483.

20 Genina, É.A., Bashkatov, A.N., Kochubey, V.I., and Tuchin, V.V. (2005) Optical clearing of human dura mater. *Opt. Spectrosc.*, **98** (3), 515–521.

21 McBride, T.O., Pogue, B.W., Poplack, S., Soho, S., Wells, W.A., Jiang, S., Osterberg, U.L., and Paulsen, K.D. (2002) Multispectral near-infrared tomography: a case study in compensating for water and lipid content in hemoglobin imaging of the breast. *J. Biomed. Opt.*, **7**, 72–79.

22 Palmer, K.F. and Williams, D. (1974) Optical properties of water in the near infrared. *J. Opt. Soc. Am.*, **64**, 1107–1110.

23 Martin, K.A. (1993) Direct measurement of moisture in skin by NIR spectroscopy. *J. Soc. Cosmet. Chem.*, **44**, 249–261.

24 Lauridsen, R.K., Everland, H., Nielsen, L.F., Engelsen, S.B., and Norgaard, L. (2003) Exploratory multivariate spectroscopic study on human skin. *Skin Res. Technol.*, **9**, 137–146.

25 Müller, G., Chance, B., Alfano, R., Arridge, S.R., Beuthan, J., Gratton, E., Kaschke, M.F., Masters, B.R., Svanberg, S., van der Zee, P. (eds) (1993) *Medical Optical Tomography: Functional Imaging and Monitoring*, vol. IS11, SPIE Press, Bellingham.

26 Tuchin, V.V., Wang, L.V., and Zimnyakov, D.A. (2006) *Optical Polarization in Biomedical Applications*, Springer-Verlag, New York.

27 Lakowicz, J.R. (1999) *Principles of Fluorescence Spectroscopy*, 2nd edn, Kluwer Academic/Plenum, New York.

28 Schneckenburger, H., Steiner, R., Strauss, W., Stock, K., and Sailer, R. (2002) Fluorescence technologies in biomedical diagnostics, in *Optical Biomedical Diagnostics*, vol. PM107 (ed. V.V. Tuchin), SPIE Press, Bellingham, pp. 827–874.

29 Sinichkin, Yu.P., Kollias, N., Zonios, G., Utz, S.R., and Tuchin, V.V. (2002) Reflectance and fluorescence spectroscopy of human skin *in vivo*, in *Optical Biomedical Diagnostics*, vol. PM107 (ed. V.V. Tuchin), SPIE Press, Bellingham, pp. 725–785.

30 Zhadin, N.N. and Alfano, R.R. (1998) Correction of the internal absorption effect in fluorescence emission and excitation spectra from absorbing and highly scattering media: theory and experiment. *J. Biomed. Opt.*, **3** (2), 171–186.

31 Drezek, R., Sokolov, K., Utzinger, U., Boiko, I., Malpica, A., Follen, M., and Richards-Kortum, R. (2001) Understanding the contributions of NADH and collagen to cervical tissue fluorescence spectra: modeling, measurements, and implications. *J. Biomed. Opt.*, **6** (4), 385–396.

32 Lucchina, L.C., Kollias, N., Gillies, R., Phillips, S.B., Muccini, J.A., Stiller, M.J., Trancik, R.J., and Drake, L.A. (1996) Fluorescence photography in the evaluation of acne. *J. Am. Acad. Dermatol.*, **35**, 58–63.

33 Soukos, N.S., Som, S., Abernethy, A.D., Ruggiero, K., Dunham, J., Lee, C., Doukas, A.G., and Goodson, J.M. (2005) Phototargeting oral black-pigmented bacteria. *Antimicrob. Agents Chemother.*, **49**, 1391–1396.

34 Schneckenburger, H., Gschwend, M.N., Sailer, R., Mock, H.P., and Straiss, W.S.L. (1998) Time-gated fluorescence microscopy in molecular and cellular biology. *Cell. Mol. Biol.*, **44**, 795–805.

35 Gannot, I., Garashi, A., Gannot, G., Chernomordik, V., and Gandjbakhche, A. (2003) *In vivo* quantitative three-dimensional localization of tumor labeled with exogenous specific fluorescence markers. *Appl. Opt.*, **42** (16), 3073–3080.

36 Ciamberlini, C., Guarnieri, V., Longobardi, G., Poggi, P., Donati, M.C., and Panzardi, G. (1997) Indocyanine green videoangiography using cooled CCD in central serous choroidopathy. *Biomed. Opt.*, **2**, 218–225.

37 Ritz, J.-P., Roggan, A., Isbert, C., Muller, G., Buhr, H., and Germer, C.-T. (2001) Optical properties of native and

coagulated porcine liver tissue between 400 and 2400 nm. *Lasers Surg. Med.*, **29**, 205–212.

38 Bashkatov, A.N., Genina, E.A., Kochubey, V.I., Kamenskikh, T.G., and Tuchin, V.V. (2009) Optical clearing of human eye sclera. *Proc. SPIE*, **7163**, 71631.

39 Stolik, S., Delgado, J.A., Pérez, A., and Anasagasti, L. (2000) Measurement of the penetration depths of red and near infrared light in human "*ex vivo*" tissues. *J. Photochem. Photobiol. B: Biol.*, **57**, 90–93.

40 Drezek, R., Dunn, A., and Richards-Kortum, R. (1999) Light scattering from cells: finite-difference time-domain simulations and goniometric measurements. *Appl. Opt.*, **38** (16), 3651–3661.

41 Sokolov, K., Drezek, R., Gossagee, K., and Richards-Kortum, R. (1999) Reflectance spectroscopy with polarized light: is it sensitive to cellular and nuclear morphology. *Opt. Express*, **5**, 302–317.

42 Askar'yan, G.A. (1982) The increasing of laser and other radiation transport through soft turbid physical and biological media. *Sov. J. Quantum Electron.*, **9** (7), 1379–1383.

43 Guzelsu, N., Federici, J.F., Lim, H.C., Chauhdry, H.R., Ritter, A.B., and Findley, T. (2003) Measurement of skin stretch via light reflection. *J. Biomed. Opt.*, **8**, 80–86.

44 Nemati, B., Dunn, A., Welch, A.J., and Rylander, H.G. III (1998) Optical model for light distribution during transscleral cyclophotocoagulation. *Appl. Opt.*, **37** (4), 764–771.

45 Lin, W.-C., Motamedi, M., and Welch, A.J. (1996) Dynamics of tissue optics during laser heating of turbid media. *Appl. Opt.*, **35** (19), 3413–3420.

46 Tuchin, V.V. (2006) *Optical Clearing of Tissues and Blood*, SPIE Press, Bellingham, PM154.

47 Rylander, C.G., Stumpp, O.F., Milner, T.E., Kemp, N.J., Mendenhall, J.M., Diller, K.R., and Welch, A.J. (2006) Dehydration mechanism of optical clearing in tissue. *J. Biomed. Opt.*, **11** (4), 041117.

48 Genina, E.A., Bashkatov, A.N., Korobko, A.A., Zubkova, E.A., Tuchin, V.V., Yaroslavsky, I.V., and Altshuler, G.B. (2008) Optical clearing of human skin: comparative study of permeability and dehydration of intact and photothermally perforated skin. *J. Biomed. Opt.*, **13** (2), 021102.

49 Bashkatov, A.N., Korolevich, A.N., Tuchin, V.V., Sinichkin, Y.P., Genina, E.A., Stolnitz, M.M., Dubina, N.S., Vecherinski, S.I., and Belsley, M.S. (2006) *In vivo* investigation of human skin optical clearing and blood microcirculation under the action of glucose solution. *Asian J. Phys.*, **15** (1), 1–14.

50 Oliveira, L., Lage, A., Clemente, M.P., and Tuchin, V. (2009) Optical characterization and composition of abdominal wall muscle from rat. *Opt. Lasers Eng.*, **47**, 667–672.

51 Huang, Y. and Meek, K.M. (1999) Swelling studies on the cornea and sclera: the effect of pH and ionic strength. *Biophys. J.*, **77**, 1655–1665.

52 Bashkatov, A.N., Genina, E.A., Sinichkin, Yu.P., Kochubey, V.I., Lakodina, N.A., and Tuchin, V.V. (2003) Glucose and mannitol diffusion in human dura mater. *Biophys. J.*, **85** (5), 3310–3318.

53 Genina, E.A., Korobko, A.A., Bashkatov, A.N., Tuchin, V.V., Yaroslavsky, I.V., and Altshuler, G.B. (2007) Investigation of skin water loss and glycerol delivery through stratum corneum. *Proc. SPIE*, **6535**, 65351.

54 Wiechers, J.W., Dederen, J.C., and Rawlings, A.V. (2009) Moisturization mechanisms: internal occlusion by orthorhombic lipid phase stabilizers – a novel mechanism of action of skin moisturization, in *Skin Moisturization* (eds A.V. Rawlings and J.J. Leyden), Taylor & Francis, pp. 309–321.

55 Genina, E.A., Bashkatov, A.N., and Tuchin, V.V. (2009) Glucose-induced optical clearing effects in tissues and blood, in *Handbook of Optical Sensing of Glucose in Biological Fluids and Tissues* (ed. V.V. Tuchin), Taylor & Francis Group LLC, CRC Press, pp. 657–692.

56 Kinnunen, M., Myllyla, R., and Vainio, S. (2008) Detecting glucose-induced changes in in vivo and in vitro experiments with optical coherence tomography. *J. Biomed. Opt.*, **13** (2), 021111.

57 Genina, E.A., Bashkatov, A.N., and Tuchin, V.V. (2008) Optical clearing of cranial bone. *Adv. Opt. Technol.*, 267867.

58 Tuchin, V.V., Maksimova, I.L., Zimnyakov, D.A., Kon, I.L., Mavlutov, A.H., and Mishin, A.A. (1997) Light propagation in tissues with controlled optical properties. *J. Biomed. Opt.*, **2**, 401–417.

59 Vargas, G., Chan, E.K., Barton, J.K., Rylander, H.G. III, and Welch, A.J. (1999) Use of an agent to reduce scattering in skin. *Lasers Surg. Med.*, **24**, 133–141.

60 Tuchin, V.V., Bashkatov, A.N., Genina, E.A., Sinichkin, Yu.P., and Lakodina, N.A. (2001) In vivo investigation of the immersion-liquid-induced human skin clearing dynamics. *Techn. Phys. Lett.*, **27** (6), 489–490.

61 Mao, Z., Zhu, D., Hu, Y., Wen, X., and Han, Z. (2008) Influence of alcohols on the optical clearing effect of skin *in vivo*. *J. Biomed. Opt.*, **13** (2), 021104.

62 Wang, R.K. and Elder, J.B. (2002) Propylene glycol as a contrasting agent for optical coherence tomography to image gastro-intestinal tissues. *Lasers Surg. Med.*, **30**, 201–208.

63 Bashkatov, A.N., Genina, E.A., and Tuchin, V.V. (2002) Optical immersion as a tool for tissue scattering properties control, in *Perspectives in Engineering Optics* (eds K. Singh and V.K. Rastogi), Anita Publications, New Delhi, pp. 313–334.

64 Yeh, A.T., Choi, B., Nelson, J.S., and Tromberg, B.J. (2003) Reversible dissociation of collagen in tissues. *J. Invest. Dermatol.*, **121**, 1332–1335.

65 Liu, H., Beauvoit, B., Kimura, M., and Chance, B. (1996) Dependence of tissue optical properties on solute – induced changes in refractive index and osmolarity. *J. Biomed. Opt.*, **1**, 200–211.

66 Leonard, D.W. and Meek, K.M. (1997) Refractive indices of the collagen fibrils and extrafibrillar material of the corneal stroma. *Biophys. J.*, **72**, 1382–1387.

67 Kon, I.L., Bakutkin, V.V., Bogomolova, N.V., Tuchin, S.V., Zimnyakov, D.A., and Tuchin, V.V. (1997) Trazograph influence on osmotic pressure and tissue structures of human sclera. *Proc. SPIE*, **2971**, 198–206.

68 Genina, E.A., Bashkatov, A.N., Sinichkin, Yu.P., and Tuchin, V.V. (2006) Optical clearing of the eye sclera in vivo caused by glucose. *Quantum Electron.*, **36** (12), 1119–1124.

69 Zimnyakov, D.A. and Sinichkin, Yu. P. (2000) A study of polarization decay as applied to improved imaging in scattering media. *J. Opt. A: Pure Appl. Opt.*, **2**, 200–208.

70 Mollee, T.R. and Bracken, A.J. (2007) A model of solute transport through stratum corneum using solute capture and release. *Bull. Math. Biol.*, **69**, 1887–1907.

71 Blank, I.H., Moloney, J., Emslie, A.G., Simon, I., and Apt, C. (1984) The diffusion of water across the stratum corneum as a function of its water content. *J. Invest. Dermatol.*, **82**, 188–194.

72 Kotyk, A. and Janacek, K. (1977) *Membrane Transport: An Interdisciplinary Approach*, Plenum Press, New York.

73 Ghanem, A.-H., Mahmoud, H., Higuchi, W.I., Liu, P., and Good, W.R. (1992) The effects of ethanol on the transport of lipophilic and polar permeants across hairless mouse skin: methods/validation of a novel approach. *Int. J. Pharm.*, **78**, 137–156.

74 Peck, K.D., Ghanem, A.-H., and Higuchi, W.I. (1994) Hindered diffusion of polar molecules through and effective pore radii estimates of intact and ethanol treated human epidermal membrane. *Pharm. Res.*, **11**, 1306–1314.

75 Jiang, J. and Wang, R.K. (2004) Comparing the synergetic effects of oleic acid and dimethyl sulfoxide as vehicles for optical clearing of skin tissue *in vitro*. *Phys. Med. Biol.*, **49**, 5283–5294.

76 Xu, X. and Zhu, Q. (2007) Evaluation of skin optical clearing enhancement with

Azone as a penetration enhancer. *Opt. Commun.*, **279**, 223–228.
77 Zhi, Z., Han, Z., Luo, Q., and Zhu, D. (2009) Improve optical clearing of skin in vitro with propylene glycol as a penetration enhancer. *J. Innovative Opt. Health Sci.*, **2** (3), 269–278.
78 Jiang, J., Boese, M., Turner, P., and Wang, R.K. (2008) Penetration kinetics of dimethyl sulphoxide and glycerol in dynamic optical clearing of porcine skin tissue in vitro studied by Fourier transform infrared spectroscopic imaging. *J. Biomed. Opt.*, **13** (2), 021105.
79 Kurihara-Bergstrom, T., Knutson, K., De Noble, L.J., and Goates, C.Y. (1990) Percutaneous absorption enhancement of an ionic molecule by ethanol–water system in human skin. *Pharm. Res.*, **7**, 762–766.
80 Williams, A.C. and Barry, B.W. (2004) Penetration enhancers. *Adv. Drug Deliv. Rev.*, **56**, 603–618.
81 Lee, S., McAuliffe, D.J., Kollias, N., Flotte, T.J., and Doukas, A.G. (2002) Photomechanical delivery of 100-nm microspheres through the stratum corneum: implications for transdermal drug delivery. *Lasers Surg. Med.*, **31**, 207–210.
82 Weigmann, H.J., Lademann, J., Schanzer, S., Lindemann, U., Pelchrzim, R.V., Schaefer, H., and Sterry, W. (2001) Correlation of the local distribution of topically applied substances inside the stratum corneum determined by tape stripping to differences in bioavailability. *Skin Pharmacol. Appl. Skin Physiol.*, **14**, 93–103.
83 Lee, W.R., Tsai, R.Y., Fang, C.L., Liu, C.J., Hu, C.H., and Fang, J.Y. (2006) Microdermabrasion as a novel tool to enhance drug delivery via the skin: an animal study. *J. Dermatol. Surg.*, **32**, 1013–1022.
84 Liu, C., Zhi, Z., Tuchin, V.V., and Zhu, D. (2009) Combined laser and glycerol enhancing skin optical clearing. *Proc. SPIE*, **7186**, 71860.
85 Stumpp, O., Welch, A.J., and Neev, J. (2005) Enhancement of transdermal skin clearing agent delivery using a 980 nm diode laser. *Lasers Surg. Med.*, **37**, 278–285.
86 Nugroho, A.K., Li, G.L., Danhof, M., and Bouwstra, J.A. (2004) Transdermal iontophoresis of rotigotine across human stratum corneum *in vitro*: Influence of pH and NaCl concentration. *Pharm. Res.*, **21** (5), 844–850.
87 Tezel, A. and Mitragotri, S. (2003) Interaction of inertial cavitation bubbles with stratum corneum lipid bilayers during low-frequency sonophoresis. *Biophys. J.*, **85**, 3502–3512.
88 Stumpp, O. and Welch, A.J. (2003) Injection of glycerol into porcine skin for optical skin clearing with needle-free injection gun and determination of agent distribution using OCT and fluorescence microscopy. *Proc. SPIE*, **4949**, 44–50.
89 Tuchin, V.V., Altshuler, G.B., Gavrilova, A.A., Pravdin, A.B., Tabatadze, D., Childs, J., and Yaroslavsky, I.V. (2006) Optical clearing of skin using flashlamp-induced enhancement of epidermal permeability. *Lasers Surg. Med.*, **38**, 824–836.
90 Yoon, J., Son, T., Choi, E., Choi, B., Nelson, J.S., and Jung, B. (2008) Enhancement of optical skin clearing efficacy using a microneedle roller. *J. Biomed. Opt.*, **13** (2), 021103.
91 Stumpp, O., Chen, B., and Welch, A.J. (2006) Using sandpaper for noninvasive transepidermal optical skin clearing agent delivery. *J. Biomed. Opt.*, **11** (4), 041118.
92 Genina, E.A., Bashkatov, A.N., Tuchin, V.V., Altshuler, G.B., and Yaroslavski, I.V. (2008) The possibility of laser tattoo removal improvement due to skin optical clearing. *Quantum Electron.*, **38**, 580–587.
93 Bashkatov, A.N., Genina, E.A., Tuchin, V.V., and Altshuler, G.B. (2009) Skin optical clearing for improvement of laser tattoo removal. *Laser Phys.*, **19** (6), 1312–1322.
94 Weiss, M., Hashimoto, H., and Nilsson, T. (2003) Anomalous protein diffusion in living cells as seen by fluorescence correlation spectroscopy. *Biophys. J.*, **84**, 4043–4052.

95 Tsai, J.-C., Lin, C.-Y., Sheu, H.-M., Lo, Y.-L., and Huang, Y.-H. (2003) Noninvasive characterization of regional variation in drug transport into human stratum corneum in vivo. *Pharm. Res.*, **20**, 632–638.

96 Schulmerich, M.V., Cole, J.H., Dooley, K.A., Morris, M.D., Kreider, J.M., and Goldstein, S.A. (2008) Optical clearing in transcutaneous Raman spectroscopy of murine cortical bone tissue. *J. Biomed. Opt.*, **13** (2), 021108.

97 Lahjomri, F., Benamar, N., Chatri, E., and Leblanc, R.M. (2003) Study of the diffusion of some emulsions in the human skin by pulsed photoacoustic spectroscopy. *Phys. Med. Biol.*, **48**, 2729–2738.

98 Bashkatov, A.N., Genina, E.A., Sinichkin, Yu.P., Kochubei, V.I., Lakodina, N.A., and Tuchin, V.V. (2003) Estimation of the glucose diffusion coefficient in human eye sclera. *Biophysics*, **48**, 292–296.

99 Marucci, M., Ragnarsson, G., and Axelsson, A. (2006) Electronic speckle pattern interferometry: a novel non-invasive tool for studying drug transport rate and drug permeability through free films. *J. Controlled Release*, **114**, 369–380.

100 Ghosn, M.G., Tuchin, V.V., and Larin, K.V. (2007) Nondestructive quantification of analyte diffusion in cornea and sclera using optical coherence tomography. *Invest. Ophthal. Vis. Sci.*, **48**, 2726–2733.

101 Larin, K.V. and Tuchin, V.V. (2009) Monitoring of glucose diffusion in epithelial tissues with optical coherence tomography, in *Handbook of Optical Sensing of Glucose in Biological Fluids and Tissues* (ed. V.V. Tuchin), Taylor & Francis Group LLC, CRC Press, pp. 623–656.

102 Bashkatov, A.N., Genina, E.A., and Tuchin, V.V. (2009) Measurement of glucose diffusion coefficients in human tissues, in *Handbook of Optical Sensing of Glucose in Biological Fluids and Tissues* (ed. V.V. Tuchin), Taylor & Francis Group LLC, CRC Press, pp. 587–621.

103 Potts, R.O., Guzek, D.B., Harris, R.R., and McKie, J.E. (1985) A noninvasive, in vivo technique to quantitatively measure water concentration of the stratum corneum using attenuated total-reflectance infrared spectroscopy. *Arch. Dermatol. Res.*, **277**, 489–495.

104 Komai, Y. and Ushiki, T. (1991) The three-dimensional organization of collagen fibrils in the human cornea and sclera. *Invest. Ophthal. Vis. Sci.*, **32**, 2244–2258.

105 Cox, J.L., Farrell, R.A., Hart, R.W., and Langham, M.E. (1970) The transparency of the mammalian cornea. *J. Physiol.*, **210**, 601–616.

106 Schmitt, J.M. and Kumar, G. (1998) Optical scattering properties of soft tissue: a discrete particle model. *Appl. Opt.*, **37**, 2788–2797.

107 Kohl, M., Esseupreis, M., and Cope, M. (1995) The influence of glucose concentration upon the transport of light in tissue-simulating phantoms. *Phys. Med. Biol.*, **40**, 1267–1287.

108 Bashkatov, A.N., Genina, E.A., Korovina, I.V., Sinichkin, Yu. P., Novikova, O.V., and Tuchin, V.V. (2001) *In vivo* and in vitro study of control of rat skin optical properties by action of 40%-glucose solution. *Proc. SPIE*, 4241, 223–230.

109 Fujimoto, J.G. and Brezinski, M.E. (2003) Optical coherence tomography imaging, in *Biomedical Photonics Handbook* (ed. T. Vo-Dinh), CRC Press, Boca Rotan, Florida.

110 Larin, K.V. and Tuchin, V.V. (2008) Functional imaging and assessment of glucose diffusion in epithelial tissues with optical coherence tomography. *Quantum Electron.*, **6**, 551–556.

111 Larin, K.V., Ghosn, M.G., Ivers, S.N., Tellez, A., and Granada, J.F. (2007) Quantification of glucose diffusion in arterial tissues by using optical coherence tomography. *Laser Phys. Lett.*, **4**, 312–317.

112 Maruo, K., Tsurugi, M., Tamura, M., and Ozaki, Y. (2003) *In vivo* nondestructive measurement of blood glucose by near-infrared diffuse-reflectance spectroscopy. *Appl. Spectrosc.*, **57**, 1236–1244.

113 Jiang, J.H., Berry, R.J., Siesler, H.W., and Ozaki, Y. (2002) Wavelength interval selection in multicomponent spectral analysis by moving window partial least-squared regression with applications to mid-infrared and near-infrared spectroscopic data. *Anal. Chem.*, **74**, 3555–3565.

114 Yaroslavsky, A.N., Neel, V., and Anderson, R.R. (2003) Demarcation of nonmelanoma skin cancer margins in thick excisions using multispectral polarized light imaging. *J. Invest. Dermatol.*, **121**, 259–266.

115 Fantini, S., Heffer, E.L., Pera, V.E., Sassaroli, A., and Liu, N. (2005) Spatial and spectral information in optical mammography. *Technol. Cancer Res. Treatment*, **4**, 471–482.

116 Gerger, A., Koller, S., Kern, T., Massone, C., Steiger, K., Richtig, E., Kerl, H., and Smolle, J. (2005) Diagnostic applicability of in vivo confocal laser scanning microscopy in melanocytic skin tumors. *J. Invest. Dermatol.*, **124**, 493–498.

117 Masters, B.R. and So, P.T.C. (2001) Confocal microscopy and multi-photon excitation microscopy of human skin *in vivo*. *Opt. Exp.*, **8**, 2–10.

118 Dickie, R., Bachoo, R.M., Rupnick, M.A., Dallabrida, S.M., DeLoid, G.M., Lai, J., DePinho R.A., and Rogers, R.A. (2006) Three-dimensional visualization of microvessel architecture of whole-mount tissue by confocal microscopy. *Microvascullar Research*, **72** (1–2), 20–26.

119 König, K. (2000) Multiphoton microscopy in life science. *J. Microsc.*, **200**, 83–104.

120 Khalil, O.S. (2004) Non-invasive glucose measurement technologies: an update from 1999 to the dawn of the new millennium. *Diabetes Technol. Therap.*, **6**, 660–697.

121 Esenaliev, R.O. and Prough, D.S. (2009) Noninvasive monitoring of glucose concentration with optical coherence tomography, in *Handbook of Optical Sensing of Glucose in Biological Fluids and Tissues* (ed. V.V. Tuchin), Taylor & Francis Group LLC, CRC Press, pp. 563–586.

122 Heise, H.M., Lampen, P., and Marbach, R. (2009) Near-infrared reflection spectroscopy for non-invasive monitoring of glucose – established and novel strategies for multivariate calibration, in *Handbook of Optical Sensing of Glucose in Biological Fluids and Tissues* (ed. V.V. Tuchin), Taylor & Francis Group LLC, CRC Press, pp. 115–156.

123 Xu, K. and Wang, R.K. (2009) Challenges and countermeasures in NIR non-invasive blood glucose monitoring, in *Handbook of Optical Sensing of Glucose in Biological Fluids and Tissues* (ed. V.V. Tuchin), Taylor & Francis Group LLC, CRC Press, pp. 281–316.

124 Qu, J. and Wilson, B.C. (1997) Monte Carlo modeling studies of the effect of physiological factors and other analytes on the determination of glucose concentration *in vivo* by near infrared optical absorption and scattering measurements. *J. Biomed. Opt.*, **2** (3), 319–325.

125 Liu, R., Chen, W., Gu, X., Wang, R.K., and Xu, K. (2005) Chance correlation in non-invasive glucose measurement using near-infrared spectroscopy. *J. Phys. D Appl. Phys.*, **38** (15), 2675–2681.

126 Maier, J.S., Walker, S.A., Fantini, S., Franceschini, M.A., and Gratton, E. (1994) Possible correlation between blood glucose concentration and the reduced scattering coefficient of tissues in the near infrared. *Opt. Lett.*, **19**, 2062–2064.

127 Bruulsema, J.T., Hayward, J.E., Farrell, T.J., Patterson, M.S., Heinemann, L., Berger, M., Koschinsky, T., Sandahal-Christiansen, J., Orskov, H., Essenpreis, M., Schmelzeisen-Redeker, G., and Böcker, D. (1997) Correlation between blood glucose concentration in diabetics and noninvasively measured tissue optical scattering coefficient. *Opt. Lett.*, **22** (3), 190–192.

128 Larin, K.V., Eledrisi, M.S., Motamedi, M., and Esenaliev, R.O. (2002) Noninvasive blood glucose monitoring with optical coherence tomography. *Diabetes Care*, **25**, 2263–2267.

129 MacKenzie, H.A., Ashton, H.S., Spiers, S., Shen, Y., Freeborn, S.S., Hannigan, J., Lindberg, J., and Rae, P. (1999) Advances in photoacoustic noninvasive glucose testing. *Clin. Chem.*, **45**, 1587–1595.

130 Kinnunen, M. and Myllyla, R. (2008) Application of optical coherence tomography, pulsed photoacoustic technique, and time-of-flight technique to detect changes in the scattering properties of a tissue-simulating phantom. *J. Biomed. Opt.*, **13** (2), 024005.

131 Kinnunen, M. and Myllyla, R. (2005) Effect of glucose on photoacoustic signals at the wavelengths of 1064 and 532 nm in pig blood and Intralipid. *J. Physics D: Appl. Phys.*, **38**, 2654–2661.

132 Von Lilienfeld-Toal, H., Weidenmuller, M., Xhelaj, A., and Mantele, W. (2005) A novel approach to non-invasive glucose measurement by mid-infrared spectroscopy: the combination of quantum cascade lasers (QCL) and photoacoustic detection. *Vib. Spectrosc.*, **38**, 209–215.

133 Hale, G. and Querry, M.R. (1973) Optical constants of water in the 200-nm to 200-nm wavelength region. *Appl. Opt.*, **12** (3), 555–563.

134 Hillson, R.M. and Hockaday, T.D. (1982) Facial and sublingual temperature changes following intravenous glucose injection in diabetics. *Diabetes Metab.*, **8**, 15–19.

135 Enejder, A.M.K., Scecina, T.G., Oh, J., Hunter, M., Shih, W.-C., Sasic, S., Horowitz, G.L., and Feld, M.S. (2005) Raman spectroscopy for noninvasive glucose measurements. *J. Biomed. Opt.*, **10**, 031114.

136 Hanlon, E.B., Manoharan, R., Koo, T.W., Shafer, K.E., Motz, J.T., Fitzmaurice, M., Kramer, J.R., Itzkan, I., Dasari, R.R., and Feld, M.S. (2000) Prospects for in vivo Raman spectroscopy. *Phys. Med. Biol.*, **45**, R1–R59.

137 McNichols, R.J. and Coté, G.L. (2000) Optical glucose sensing in biological fluids: an overview. *J. Biomed. Opt.*, **5**, 5–16.

138 Plotnikov, S., Juneja, V., Isaacson, A.B., Mohler, W.A., and Campagnola, P.J. (2006) Optical clearing for improved contrast in second harmonic generation imaging of skeletal muscle. *Biophys. J.*, **90**, 328–339.

139 LaComb, R., Nadiarnykh, O., Carey, S., and Campagnola, P.J. (2008) Quantitative second harmonic generation imaging and modeling of the optical clearing mechanism in striated muscle and tendon. *J. Biomed. Opt.*, **13** (2), 021109.

140 Yasui, T., Tohno, Y., and Araki, T. (2004) Characterization of collagen orientation in human dermis by two-dimensional second-harmonic-generation polarimetry. *J. Biomed. Opt.*, **9** (2), 259–264.

141 Cicchi, R., Pavone, F.S., Massi, D., and Sampson, D.D. (2005) Contrast and depth enhancement in two-photon microscopy of human skin *ex vivo* by use of optical clearing agents. *Opt. Express*, **13** (7), 2337–2344.

142 Cicchi, R., Sestini, S., De Giorgi, V., Massi, D., Lotti, T., and Pavone, F.S. (2008) Nonlinear laser imaging of skin lesions. *J. BioPhotonics*, **1** (1), 62–73.

143 de Boer, J.F., Milner, T.E., and Nelson, J.S. (1999) Determination of the depth resolved Stokes parameters of light backscattered from turbid media using polarization sensitive optical coherence tomography. *Opt. Lett.*, **24**, 300–302.

144 de Boer, J.F. and Milner, T.E. (2002) Review of polarization sensitive optical coherence tomography and Stokes vector determination. *J. Biomed. Opt.*, **7** (3), 359–371.

145 Sharpe, J. (2004) Optical projection tomography. *Annu. Rev. Biomed. Eng.*, **6**, 17.1–17.20.

146 Sharpe, J., Ahlgren, U., Perry, P., Hill, B., Ross, A., Hecksher-Sørensen, J., Baldock, R., and Davidson, D. (2002) Optical projection tomography as a tool for 3D microscopy and gene expression studies. *Science*, **296**, 541–545.

147 Wang, J., Zhi, Z., Han, Z., Liu, C., Mao, Z., Wen, X., and Zhu, D. (2009) Accessing the structure and function information of deep skin blood vessels with noninvasive optical method. *Proc. SPIE*, **7176**, 71760Q–71760Q8.

148 Vargas, G., Barton, J.K., and Welch, A.J. (2008) Use of hyperosmotic chemical agent to improve the laser treatment of cutaneous vascular lesions. *J. Biomed. Opt.*, **13** (2), 021114.

149 Khan, M.H., Chess, S., Choi, B., Kelly, K.M., and Nelson, J.S. (2004) Can topically applied optical clearing agents increase the epidermal damage threshold and enhance therapeutic efficacy? *Lasers Surg. Med.*, **35**, 93–95.

150 McNichols, R.J., Fox, M.A., Gowda, A., Tuya, S., Bell, B., and Motamedi, M. (2005) Temporary dermal scatter reduction: quantitative assessment and implications for improved laser tattoo removal. *Lasers Surg. Med.*, **36**, 289–296.

151 Ross, E.V., Yashar, S., Michaud, N., Fitzpatrick, R., Geronemus, R., Tope, W.D., and Anderson, R.R. (2001) Tattoo darkening and nonresponse after laser treatment. *Arch. Dermatol.*, **137**, 33–37.

152 Prinz, B.M., Vavricka, S.R., Graf, P., Burg, G., and Dummer, R. (2004) Efficacy of laser treatment of tattoos using lasers emitting wavelengths of 532 nm, 755 nm and 1064 nm. *Br. J. Dermatol.*, **150**, 245–251.

153 Huzaira, M. and Anderson, R. (2002) Magnetite tattoos. *Lasers Surg. Med.*, **31**, 121–128.